

[Click here to view linked References](#)

1                   **Mid-Holocene to present-day evolution of the Indian monsoon**  
2                   **in transient global simulations**

3  
4  
5   Julien Crétat<sup>1,2,\*</sup>, Pascale Braconnot<sup>1</sup>, Pascal Terray<sup>3</sup>, Olivier Marti<sup>1</sup> and Fabrizio Falasca<sup>4</sup>

6  
7  
8   1 IPSL/Laboratoire des Sciences du Climat et de l'Environnement, CEA-CNRS-UVSQ,  
9   Université Paris Saclay, Gif-sur-Yvette, France

10  
11   2 Biogéosciences/CRC, CNRS-UB, Université de Bourgogne, Dijon, France

12  
13   3 IPSL/Laboratoire d'océanographie et du climat : expérimentations et approches numériques,  
14   Sorbonne Universités-CNRS-IRD-MNHN, Université Paris 6, Paris, France

15  
16   4 School of Earth and Atmospheric Sciences, Georgia Institute of Technology, Atlanta, GA  
17   30332, USA

18  
19  
20  
21  
22  
23                   *Submitted to Climate Dynamics*

24                   28/02/2020

25  
26                   Revised

27                   04/06/2020

28  
29  
30  
31  
32   \* Now at Science Partners, Paris, France

33  
34   Correspondance to [julien.cretat@science-partners.com](mailto:julien.cretat@science-partners.com)

35 **Abstract**

36

37 The low-frequency evolution of Indian rainfall mean-state and associated interannual-to-  
38 decadal variability is discussed for the last 6000 years from a multi-configuration ensemble of  
39 fully coupled global transient simulations. This period is marked by a shift of Indian Summer  
40 Monsoon Rainfall (ISMR) distribution towards drier conditions, including extremes, and a  
41 contraction of the rainy season. The drying is larger in simulations with higher horizontal  
42 resolution of the atmosphere and revised land surface hydrology. Vegetation-climate  
43 interactions and the way runoff is routed to ocean modulate the timing of the monsoon onset  
44 but have negligible effects on the evolution of seasonal rainfall amounts in our modeling  
45 framework in which carbon cycling is always active. This drying trend is accompanied by  
46 changes in ISMR interannual-to-decadal variability decreasing over north and south India but  
47 increasing over central India (20°-25°N).

48

49 The ISMR interannual-to-decadal variability is decomposed into six physically consistent  
50 regimes using a clustering technique to further characterize its changes and associated  
51 teleconnections. From 6 to 3.8 kyr BP, the century-to-century modulations in the frequency of  
52 occurrence associated to the regimes are asynchronous between the simulations. Orbitally-  
53 driven trends can only be detected for two regimes over the whole 6 kyr BP to 0 kyr BP period.  
54 These two regimes reflect increased influence of ENSO on both ISMR and Indian Ocean Dipole  
55 as the inter-hemispheric energy gradient weakens. Severe long-term droughts are also shown  
56 to be a combination of long-term drying and internally generated low-frequency modulations  
57 of the interannual-to-decadal variability.

58

59 **Keywords:** Holocene, Indian Summer Monsoon, internal variability, orbital forcing, rainfall  
60 mean-state and variability, transient simulations

61

## 62 **1. Introduction**

63

64 The Indian Summer Monsoon Rainfall (ISMR) provides about 80% of the annual rainfall  
65 amounts over India from June to September (JJAS) with significant variability on a wide range  
66 of timescales (Roxy and Chaithra 2018). Since ISMR variations profoundly impact on  
67 livelihood, which mostly relies on rain-fed agriculture (Kesava Rao et al. 2020), improved  
68 understanding of multi-scale ISMR variations is thus critical to reduce society vulnerability to  
69 climate change and extremes. Two ranges of natural variability, interannual and decadal  
70 timescales, are critical for adaptation planning and long-term mitigation.

71

72 At the interannual timescale, the El Niño Southern Oscillation (ENSO; Philander 1983) and the  
73 Indian Ocean Dipole (IOD; Saji et al. 1999) are the two main modes of ocean-atmosphere  
74 variability affecting ISMR. El Niño events are associated with an eastward shift of the Walker  
75 circulation in the Indo-Pacific sector, which induces subsidence and dry conditions over India,  
76 and *vice versa* during La Niñas (Walker 1924; Sikka 1980; Rasmusson and Carpenter 1983;  
77 Wang et al. 2005). Positive IODs are associated with warm sea surface temperature (SST)  
78 anomalies in the western tropical Indian Ocean (IO) and cold SST anomalies in the eastern  
79 equatorial IO coupled to low-level easterly wind anomalies along the equatorial IO. Positive  
80 IODs favor the existence of a reversed regional Hadley cell that enhances rainfall over India,  
81 and *vice versa* for negative IODs (Ashok et al. 2001, 2004; Gadgil et al. 2004; Ashok and Saji  
82 2007). However, positive IODs are often triggered by El Niños and negative IODs by La Niñas  
83 (Behera et al. 2006). It is therefore nontrivial to disentangle the effects of both ENSO and IOD  
84 on ISMR from observations alone. At the decadal time scale, ISMR is modulated by the Pacific  
85 Decadal Oscillation (PDO; Mantua et al. 1997; Joshi and Kucharski 2017). A negative/positive  
86 phase of the PDO promotes wet/dry ISMR anomalies. Additionally, a further amplification of  
87 this link has been found when PDO and ENSO are in phase (Krishnan et al. 2003; Roy et al.

88 2003; Krishnamurthy and Krishnamurthy 2013; Malik et al. 2017; Malik and Brönnimann  
89 2018). Finally, the Atlantic Multidecadal Oscillation (Enfield et al. 2001) can also influence  
90 ISMR (e.g., Malik et al. 2017; Malik and Brönnimann 2018).

91

92 The extent to which low-frequency modes of variability modulate ISMR variability at  
93 interannual-to-decadal timescales is still an open question. The ISMR long-term fluctuations  
94 have been related to changes in solar radiations induced by changes in Earth's orbit. For  
95 example, mid- to late Holocene changes in orbital configuration weaken the inter-hemispheric  
96 energy gradient as well as land-sea and moist static energy contrasts (e.g., Kutzbach 1981;  
97 Joussaume et al. 1999). This leads to a decrease and southward shift of boreal summer  
98 monsoons in both observations (e.g., Bartlein et al. 2011) and models (e.g., Liu et al. 2003;  
99 Zhao et al. 2005; Braconnot et al. 2007a-b; Marzin and Braconnot 2009; Zhao and Harrison  
100 2012; Harrison et al. 2015). Also, modeling studies have shown that the buildup of a seasonal  
101 IOD-like pattern in autumn contributes to delay the monsoon withdrawal during the mid-  
102 Holocene (Zhao et al. 2005; Braconnot et al. 2007).

103

104 Paleo reconstructions reveal that the mid- to late Holocene drying trend of ISMR is punctuated  
105 by long periods of anomalously high/low rainfall that are not necessarily phased in time across  
106 India (e.g., Kathayat et al. 2016, 2017; Kaushal et al. 2018; Kumar et al. 2019), as well as mega-  
107 droughts such as the 4.2 kyr BP event (Staubwasser et al. 2003; Giesche et al. 2019). These  
108 studies suggest that regional changes in ISMR can often result from the highly nontrivial  
109 interplay between internal variability and external forcing of the system.

110

111 Paleo-reconstruction archives are clues for characterizing and understanding past climates.  
112 However, their spatial coverage and temporal resolution remain often too low or inconstant

113 over time to easily address changes in the interannual-to-decadal ISMR variability and  
114 associated teleconnections during the Holocene. Transient global simulations run with general  
115 circulation models are thus complementary tools to investigate ISMR evolution. Until recently,  
116 such simulations were performed using accelerated changes in orbital forcing (Lorenz et al.  
117 2004, 2006; Varma et al. 2012) because of huge computational constraints. This protocol does  
118 not allow us to examine the rhythm of changes nor interannual-to-decadal variability since  
119 orbital forcing is accelerated by a factor 10 to 100 (Varma et al. 2016). Long transient  
120 simulations performed with Earth System models and yearly-updated orbital forcing (Liu et al.  
121 2009; Jungclaus 2011) offer new possibilities to overcome these limitations since they provide  
122 a thorough spatio-temporal continuum of climate evolution. Such simulations have been used  
123 successfully to discuss the evolution of the Asian and African monsoons during the Holocene  
124 (Dallmeyer et al. 2015, 2019; Shi and Yan 2019; Jalihal et al. 2019), their multi-scale changes  
125 and teleconnections (Braconnot et al. 2019a-b), or mega-drought during the 4.2 ka BP event  
126 (Yan and Liu 2019). They are also tailored for the investigation of the complex spatio-temporal  
127 interrelationships in the ENSO-IOD-ISMR system.

128

129 In this study, we build on the work of Braconnot et al. (2019b), who show that ISMR  
130 interannual-to-decadal variability increases from mid- to late Holocene due to increased ENSO  
131 variability in two 6000-yr transient simulations ran with the IPSL (Institut Pierre et Simon  
132 Laplace) Earth system model. Here, we consider a multi-configuration ensemble of transient  
133 simulations to refine their results. We investigate the effects of horizontal resolution, land  
134 hydrology, vegetation and runoff on changes in ISMR, with a focus on its seasonality at the  
135 monthly timescale and on its probability density function and extremes at the seasonal  
136 timescale. We also investigate changes in the interannual-to-decadal variability of ISMR and  
137 its teleconnections based on a clustering approach. Our aim is to highlight regional patterns in

138 ISMR interannual changes and to assess the temporal stability of ISMR teleconnections in the  
139 transient simulations. The results of these analyses should also provide guidance to design  
140 appropriate model-data comparison to analyze monsoon variability when dealing with a wide  
141 range of spatio-temporal timescales.

142

143 Section 2 describes the simulations and the methodology used. Section 3 gives an overview of  
144 trends in Indian rainfall seasonality, probability density function and extremes. Section 3 also  
145 analyzes the rhythm and spatial consistency of changes at the local scale over the Indian sector.  
146 Section 4 investigates changes in ISMR interannual-to-decadal variability and its  
147 teleconnections through the regime approach with a focus on 6–3.8 kyr BP and discusses the  
148 robustness of our results. Section 5 summarizes the results and gives the main conclusions.

149

150

## 151 **2. Model simulations and methodology**

152

### 153 2.1 The IPSL model

154

155 We consider two model versions of the IPSL Earth System model (Table 1). The first one,  
156 called TR5A hereafter, is the IPSL-CM5A model version used for the CMIP5 ensemble of past,  
157 present and future simulations (Dufresne et al. 2013; Mignot and Bony 2013) and modified by  
158 Sepulchre et al. (2019). TR5A couples atmosphere, land surface, ocean and sea-ice, and  
159 accounts for energy, water and carbon cycles. The second version, called TR6A hereafter,  
160 includes a new 11-layer hydrological model, a prognostic 3-layer snow model and the  
161 possibility to switch on a dynamical vegetation component (Braconnot et al. 2019a). In both  
162 model versions, the vegetation in each grid box is represented by 13 Plant Functional Types

163 (PFTs) and carbon cycle is interactive. The leaf area index (LAI) is thus fully interactive and  
164 varies depending on energy, water and carbon cycles regardless of the model version. When  
165 vegetation is prescribed, the 13 PFTs are assigned to a fixed land cover map. When vegetation  
166 is computed, only natural vegetation is accounted for and the distribution of the 13 PFTs in  
167 each model grid cell varies with time.

168

169 The resolution of the atmosphere is  $3.75^\circ \times 1.875^\circ$  for TR5A and  $2.5^\circ \times 1.25^\circ$  for TR6A on the  
170 horizontal and 39 levels for the two versions on the vertical. For ocean, TR5A and TR6A share  
171 the same  $2^\circ$  ORCA configuration (Madec et al. 2017), with a tri-polar grid, mesh refinement at  
172 the equator and 31 vertical levels. River and direct runoff are routed to the corresponding ocean  
173 coastal grid box. Specific schemes connect snow accumulation over the ice sheet and endorheic  
174 basins to the ocean (Marti et al. 2010) to ensure a perfect closure of the water cycle. The  
175 corresponding algorithm now uses a full parallel version of the interpolation weights between  
176 the land-atmosphere and ocean grids. The parameters of the new algorithm were chosen to  
177 produce similar results as before. This new version of the land-ocean runoff is called CM6 in  
178 Table 1.

179

## 180 2.2 Transient simulations

181

182 An ensemble of five transient simulations is performed with yearly changes in orbital  
183 parameters and trace gases following the protocol proposed by Otto-Bleisner et al. (2017). This  
184 ensemble accounts for differences in model resolution, the representation of land-surface  
185 hydrology, snow and river runoff, as well as dynamical vegetation. Details on major  
186 components of each simulation can be found in Table 1.

187

188 Two simulations, TR5AS-Vlr01 and TR6AV-Sr02 span the time range from 6 to 0 kyr BP  
189 (Braconnot et al. 2019a-b), with 0 kyr BP corresponding to 1950 Common Era. The remaining  
190 simulations also start at 6 kyr BP but are 4000-yr or 2250-yr long integrations (Table 1).

191

192 The TR5AS-Vlr01 is run with the TR5A model version and with vegetation prescribed to the  
193 IPSL-CM5A 1850 reference map (Dufresne et al. 2013). The other simulations are run with the  
194 TR6A model version. The TR6AV-Sr02 simulation has dynamical vegetation. The TR6AS-  
195 Sr10 and TR6AS-Sr12 simulations are similar to TR6AV-Sr02, except that vegetation is  
196 prescribed to the 1850 reference map for the former and to the mid-Holocene natural vegetation  
197 as computed by the model for the latter (Table 1). An error was found in the first release of the  
198 interpolation weights, which might affect the results of the TR6AV-Sr02, TR6AS-Sr10 and  
199 TR6AS-Sr12 simulations (Table 1). In these simulations, a fraction of the river and direct runoff  
200 is redistributed globally and not at the river mouth (“inter” in Table 1). This doesn’t affect the  
201 water closure of the model, but the ocean regional circulation. A simulation similar to TR6AS-  
202 Sr10, called TR6AS-Sr11 (Table 1), was thus run to test the effect of this bug (“inter”)  
203 compared to the CM6 land-ocean river runoff.

204

205 The different model versions and model setups produce slightly different mean climate and  
206 climate characteristics (Braconnot et al. 2019a). To avoid any spurious drift at the beginning of  
207 the transient simulations that would arise from an initial shock, the initial state for each transient  
208 simulation results from a 1,000-yr long mid-Holocene simulation (i.e., with Earth’s orbit and  
209 trace gases prescribed to mid-Holocene values and kept constant throughout the simulation)  
210 performed with the corresponding version of the model. The initial states are thus entirely  
211 consistent with the mid-Holocene climate simulated by each model configuration, ensuring no  
212 artificial model drift at the beginning of the transient simulations.



213

### 214 2.3 Statistical analysis of Indian rainfall and teleconnections

215

216 Complementary analyses allow us to characterize the long-term evolution of ISMR and of its  
217 variability. We first use a rainfall index area-averaged over India (land points within  $5^{\circ}$ - $25^{\circ}$ N  
218 and  $77^{\circ}$ - $88^{\circ}$ E) to assess changes in (i) the seasonality of the Indian rainfall mean-state and its  
219 variability at the monthly timescale, (ii) the probability density function of seasonal ISMR  
220 amounts during boreal summer (i.e., JJAS) and (iii) extreme ISMR years (i.e., flood and drought  
221 years). This domain embeds regions strongly affected by boreal summer Indian monsoon.  
222 Analyses are performed considering 100-yr adjacent windows from 6 kyr BP onwards. Rainfall  
223 mean-state is defined as the average within each 100-yr window, while rainfall variability is  
224 defined either as the standard-deviation within each window or as anomalies with respect to the  
225 mean-state estimated in the window. The 100-yr length of the windows is retained to focus on  
226 interannual-to-decadal variability. The century-to-century evolution of these descriptors will be  
227 interpreted as centennial-to-multicentennial modulation of rainfall mean-state and interannual-  
228 to-decadal variability.

229

230 To account for potential spatial disparity in the ISMR evolution that are hidden in the area-  
231 averaged index, we then adopt a “regime” approach based on the Agglomerative Hierarchical  
232 Clustering (AHC; Gong and Richman 1995). This technique, presented in Appendix A, is  
233 retained to detect recurrent anomalous rainfall patterns over India at the interannual-to-decadal  
234 timescale. It is preferred to Empirical Orthogonal Function analysis because it allows us to  
235 highlight regional nuances without imposing artificial north–south or west–east structures  
236 induced by orthogonality relationships and to account for nonlinearities in the teleconnection  
237 between (wet and dry) ISMR regimes and ENSO.

238

239 For the AHC analyses, anomalies of JJAS rainfall patterns are computed for each adjacent 100-  
240 yr window as the departures from the corresponding rainfall mean-state inside the window. The  
241 AHC is fed by the 5 simulations simultaneously to focus on the shared signals across the  
242 simulations. The AHC provides a hierarchy of clusters from  $N$  to 1, with  $N$  being the total  
243 number of classified (time) patterns. The patterns are grouped based on their similarity and to  
244 minimize intra-cluster variance and maximize inter-cluster variance. The optimal number of  
245 ISMR regimes (i.e., clusters) is a compromise between the intra- and inter-cluster variance and  
246 the physical meaning of the identified clusters. Here, we detect 6 ISMR regimes using different  
247 metrics (see Appendix A for details). The 6 ISMR regimes are then characterized by computing  
248 their center of gravity, that is, by averaging all anomalous patterns in JJAS rainfall, diverse  
249 atmospheric fields and SST belonging to each regime. Their robustness is assessed through  
250 statistics to test whether or not the centers of gravity of the regimes differ significantly from the  
251 center of gravity of the whole population (Student t-test at the 95% confidence level) and by  
252 discussing the similarity between them and those associated to each simulation (e.g., the center  
253 of gravity of all patterns of TR5AS-Vlr01 belonging to regime #1).

254

#### 255 2.4 Representation of the Indian monsoon by the IPSL model

256

257 The two model versions reasonably capture the mid-Holocene wetting of the Northern  
258 Hemisphere monsoon regions (Kageyama et al. 2013a-b; Braconnot et al. 2019a) and the  
259 teleconnection between the Indian monsoon and ENSO at the interannual timescale during the  
260 recent period (Braconnot et al. 2019b). Here, their ability in capturing both the mean-state and  
261 interannual-to-decadal variability of Indian rainfall is assessed for modern conditions against  
262 three observational monthly products: the All Indian Rainfall index (AIR; Parthasarathy et al.

263 1995), which is an area-weighted average of 306 rain gauges distributed across India from 1871  
264 onwards, and the GPCP version 2.2 (Adler et al. 2003) and CRU-TS4.01 (Harris et al. 2014)  
265 data.

266

267 Regarding rainfall mean-state, the magnitude of the monsoon peak and JJAS amounts is close  
268 to observations in TR6AV-Sr02, while depicts a  $\sim 2$  mm/day dry bias in TR5AS-Vlr01 (Fig. 1a  
269 and Table 2). The latter dry bias is typical of low-resolution global coupled simulations (Sperber  
270 et al. 2013; Goswami and Goswami 2017; Terray et al. 2018). The improvement of TR6AV-  
271 Sr02 on TR5AS-Vlr01 is due to a better penetration of the monsoon flow along the Himalaya  
272 foothill induced by increased horizontal resolution (Fig. 2) and to increased local recycling  
273 induced by the 11-layer hydrology model (Braconnot et al. 2019a). On the other hand,  
274 horizontal resolution and hydrology do not affect the onset and demise phases of the Indian  
275 monsoon, which are similar between the two model's versions. The fast withdrawal observed  
276 between September and October is accurately captured, while the onset observed in June is  
277 delayed by 1 month in the simulations (Fig. 1a). The 1-month delay in the onset results from a  
278 too slow northwestward propagation of the rain belt during early summer over India (Fig. 2).  
279 This slow propagation involves a too late inversion of the meridional tropospheric temperature  
280 gradient between landmass and the IO due to a persistent cold bias over the Himalayas (Marzin  
281 and Braconnot 2009) and Indo-Pacific SST biases intrinsic to ocean-atmosphere coupled  
282 simulations (Sperber et al. 2013; Prodhomme et al. 2015). Note, however, that the northernmost  
283 extent of the monsoon in August and September is consistent with observations (Fig. 2).

284

285 Regarding rainfall variability, the observations depict a plateau of  $1.5 \text{ mm.day}^{-1}$  from June to  
286 September when considering the standard-deviation of the long time series in the AIR and CRU  
287 data (Fig. 1b). This plateau hides large observed variability of the monsoon onset and demise

288 when considering 20-yr long time series (see GPCP and thin curves for AIR in Fig. 1b). This  
289 double peak is captured by the two simulations despite a clear 1-month delay of the first peak  
290 linked to the aforementioned bias in the mean-state and exaggerated magnitude, especially in  
291 the TR6AV-Sr02 (Fig. 1b and Table 2, second column).

292

293

### 294 **3. Trends in seasonality and boreal summer Indian monsoon rainfall**

295

#### 296 3.1 Evolution of Indian rainfall seasonality

297

298 The evolution of Indian rainfall seasonality, estimated in 100-yr adjacent windows, is affected  
299 by the insolation and trace gas forcing (Fig. 3). The TR5AS-Vlr01 and TR6AV-Sr02 depict  
300 decreased monthly rainfall amounts throughout the seasonal cycle and reduced length of the  
301 Indian monsoon season from mid- to late Holocene (Fig. 3a-b), with delayed onset and early  
302 withdrawal. The delayed onset is not affected by the calendar effect induced by changes in  
303 orbital forcing in early boreal summer when the vernal equinox is set to March 21 in all  
304 simulations (Joussaume and Braconnot 1997; Bartlein and Shafer 2019). Daily output would  
305 be required to fully assess the calendar effect on the early withdrawal since this effect is  
306 maximal in late boreal summer with the calendar reference used here. However, the reduced  
307 length of the Indian monsoon is consistent with Marzin and Braconnot (2009). These authors  
308 analyzed daily values and suggested that the gradual warming of the tropical ocean and cooling  
309 of the Northern Hemisphere late summer SST throughout the Holocene are the main drivers of  
310 the reduced length of the Indian monsoon from mid- to late Holocene. Despite the drying trend  
311 in rainfall mean-state (Fig. 3a-b), TR5AS-Vlr01 and TR6AV-Sr02 simulate increased  
312 interannual-to-decadal variability with time, in June-July for TR5AS-Vlr01, but for all

313 monsoon months in TR6AV-Sr02 (Fig. 3c-d). The opposite trends between rainfall mean-state  
314 and rainfall variability highlight the need to carefully untangle mean-state and variability  
315 evolutions in climate change studies.

316

317 The broad features of rainfall mean-state seasonality of the other simulations are close to  
318 TR6AV-Sr02. It is, however, worth noting that vegetation-climate feedbacks and the way river  
319 runoff is routed to ocean have significant impacts on the onset and early part of the Indian  
320 monsoon (Fig. 3e-h). These results are consistent with the sensitivity experiments of Sooraj et  
321 al. (2019), who have demonstrated that albedo perturbations play a significant role on the Indian  
322 monsoon during the first part of the rainy season (e.g. June-July), while convective processes  
323 dominate ISMR afterward. The simulation with “inter” river runoff (TR6AS-Sr10: Fig. 3e) is  
324 much wetter in June-July than the simulation with CM6 runoff (TR6AS-Sr11: Fig. 3f). In  
325 addition, the simulation with prescribed 1850 vegetation (TR6AS-Sr10: Fig. 3e) is wetter in  
326 June and drier in July than the simulations with prescribed mid-Holocene vegetation (TR6AS-  
327 Sr12: Fig. 3g) or dynamical vegetation (TR6AV-Sr02: Fig. 3h). Finally, the use of a fixed  
328 vegetation map in TR6AS-Sr12 induces a significant shift of ISMR from the second half to the  
329 first part of the rainy season from 6 to 3.8 kyr BP (Fig. 3e), but this specific time evolution is  
330 not simulated with a dynamical vegetation in TR6AV-Sr02. A dedicated study is needed to  
331 understand the mechanisms by which vegetation-climate feedbacks and river runoff affect the  
332 Indian monsoon onset. The interannual-to-decadal variability remains very noisy from one  
333 TR6A simulation to another from 6 to 3.8 kyr BP (not shown), highlighting the chaotic nature  
334 of this range of variability.

335

336 3.2 Pace of change in Indian summer monsoon rainfall

337

338 We now consider JJAS seasonal averages to assess the pace and magnitude of changes in  
339 rainfall mean-state and variability during the Holocene. The JJAS season is chosen to  
340 encompass differences in Indian rainfall amounts arising from changes in both the amplitude  
341 and length of the monsoon with time. The Probability Density Function (PDF) of JJAS rainfall  
342 amounts shifts towards lower values from mid- to late Holocene in the two 6000-yr long  
343 simulations (Fig. 4a-b). While the shape of the PDF barely varies along the period in the  
344 TR5AS-Vlr01 (Fig. 4a), it flattens and is more skewed to the left towards present-day  
345 conditions in TR6AV-Sr02 (Fig. 4b). This reflects stronger changes in ISMR interannual-to-  
346 decadal variability in the TR6AV-Sr02 than the TR5AS-Vlr01.

347

348 Both experiments simulate changes that are more significant for the 10% driest than 10%  
349 wettest seasons estimated through a percentile approach (Fig. 4c). This confirms that the drying  
350 concerns not only the center of the distribution, but also the drought years, which become more  
351 severe towards present-day climate, especially in TR6AV-Sr02. The evolution in the number  
352 of extreme ISMR seasons in each simulation (and not on each 100-yr window extracted from  
353 the simulations) highlights that the drying trend in ISMR mean-state results also from increased  
354 occurrence of droughts (Fig. 4d) rather than decreased occurrence of floods (Fig. 4e). This result  
355 is very robust across the 5 simulations and is thus interpreted as a response to orbital forcing.  
356 Note that the magnitude of changes is weaker in TR5AS-Vlr01 than the other simulations,  
357 especially after 4 kyr BP (Fig. 4d).

358

359 The evolution in the intensity and, to a greater extent, frequency of the driest and wettest JJAS  
360 seasons depicts large inter-centennial fluctuations (Fig. 4c-e). The most striking example is the  
361 evolution of the 10% driest ISMR seasons with up to 500 consecutive years depicting increase  
362 or decrease in their occurrence (Fig. 4d). Associated changes exceed, by far, the magnitude of

363 the trend simulated for the last 6000 years. Such events are independent from orbital forcing  
364 since they are not synchronized between the simulations and occur at any time during the last  
365 6000 years (Braconnot et al. 2019b).

366

### 367 3.3 Broader context of boreal summer changes

368

369 The broader context of JJAS changes in 100-yr mean-state and associated interannual-to-  
370 decadal variability is now analyzed in the framework of Indo-Pacific rainfall and SST patterns  
371 to provide a more comprehensive view of ISMR changes (Figs. 5-6). We focus the discussion  
372 on the aspects that emerge in all simulations but show the results only for the TR6AV-Sr02  
373 from 6 to 0 kyr BP.

374

375 Compared to 6-5.9 kyr BP, significant dry rainfall anomalies emerge over the Himalayas, and  
376 immediately east of the western Ghats as soon as 5.9-5.5 kyr BP. They rapidly expand over all  
377 India and grow in intensity afterwards (Fig. 5; contours). This drying reflects the direct response  
378 of the Indian monsoon to the orbitally-driven weakening (strengthening) of seasonality in the  
379 Northern (Southern) Hemisphere (Braconnot et al. 2007a). It is associated to progressive SST  
380 cooling in most regions of the Northern Hemisphere and SST warming in the Southern  
381 Hemisphere (Fig. 6; contours). Over the IO, anomalous SSTs reflect a combination of these  
382 orbitally-driven global forcing and of changes in monsoon circulation (Zhao et al. 2005). The  
383 negative rainfall anomalies trend over the IO between the Equator and 8°N (Fig. 5) is a key  
384 feature that emerges also in coral-based reconstructions (Abram et al. 2007) and is coupled to  
385 a shift towards negative IOD conditions in simulated SST patterns (Fig. 6).

386

387 The pattern of changes in rainfall variability (Fig. 5; shadings) is well correlated to the pattern

388 of changes in rainfall mean-state (Fig. 5; contours). Regions experiencing a drying trend are  
389 characterized by decreased variability, and *vice versa*. The only exception is central India  
390 (between 20°N and 25°N) where rainfall mean-state decreases but rainfall variability starts  
391 increasing after 3 kyr BP and keeps increasing until late Holocene (Fig. 5; shadings). The  
392 increased rainfall variability over central India is embedded in a pattern extending from the  
393 northeastern part of the Arabian Sea to the Bay of Bengal. This suggests a coherent large-scale  
394 amplitude variation of the monsoon trough over land and ocean in the IO region. Moisture  
395 convergence into central India and the monsoon trough becomes thus more variable with time.  
396 This also indicates that the increased variability of area-averaged Indian rainfall discussed in  
397 Braconnot et al. (2019b) reflects the behavior of central India.

398

399 Contrary to rainfall, the pattern of changes in SST variability (Fig. 6; shadings) does not  
400 resemble that of changes in SST mean-state (Fig. 6; contours). For the mean-state, the main  
401 tropical features in the simulations are the emergence of a well-defined cold tongue along the  
402 Equator in the eastern Pacific and eastern Atlantic and of a negative IOD-like SST pattern in  
403 the IO. Consistent with these mean-state changes and slow adjustments by ocean dynamics,  
404 SST variability increases in the central-to-eastern equatorial Pacific (e.g. enhanced ENSO  
405 variability) and the eastern equatorial Atlantic, but decreases in the eastern equatorial IO (off  
406 Java). Interestingly, the SST variability is enhanced in the western tropical IO, despite the  
407 decreased SST variability in the eastern tropical IO. This suggests that IOD modulations are  
408 not the main trigger of these changes of variability over the western IO. To sum up, these mid-  
409 to late Holocene changes of tropical SST are consistent with the amplification (cooling) of the  
410 Pacific and Atlantic upwelling (Braconnot et al. 2012), increased ENSO variability reported  
411 during the Holocene (Emile-Geay et al. 2016) and a strong control of ENSO on tropical IO SST  
412 variability, especially the western IO, as seen in present-day climate (Crétat et al. 2017).



413

#### 414 **4. Changes in recurrent ISMR regimes and teleconnections**

415

416 We now go one step further by analyzing ISMR interannual-to-decadal variability no more as  
417 a standard-deviation around the mean-state but through six recurrent ISMR regimes extracted  
418 from a cluster analysis of Indian rainfall anomalies with respect to the mean-state estimated in  
419 100-yr windows (see Appendix A for details). The ISMR regimes are mainly discussed from 6  
420 to 3.8 kyr BP within the 5-simulation ensemble to account for uncertainties induced by the  
421 model versions and setups. They are also briefly discussed for late Holocene and from mid- to  
422 late Holocene within the two 6000-yr long simulations to assess model skill and long-term  
423 trends in rainfall interannual-to-decadal variability, respectively.

424

##### 425 4.1 Ensemble mean

426

427 Regimes #1 and #6 represent respectively ~14% and ~26% of the JJAS anomalous Indian  
428 rainfall patterns classified from 6 to 3.8 kyr BP (Table 3; 1<sup>st</sup> column). They both describe a  
429 weak meridional dipole in rainfall anomalies over India (Fig. 7a,f) associated with modest SST  
430 anomalies in the tropics (Fig. 8a,f). Regime #1 consists in significant wet and dry rainfall  
431 anomalies in central and south India, respectively (Fig. 7a). Regime #6 depicts a similar dipole  
432 structure but slightly shifted northward (Fig. 7f: wet/dry anomalies north/south of ~15°N).  
433 Regime #1 is associated with warm tropical Pacific SST anomalies and cold North subtropical  
434 SST anomalies in the three basins (Fig. 8a). This weakens the meridional temperature gradient,  
435 hence limiting westerly wind anomalies over the Arabian Sea (Fig. 9a). On the other hand, the  
436 increased meridional temperature gradient in regime #6 strengthens westerly wind anomalies  
437 over Africa and North Africa and favors a northwestward shift of the monsoon trough over

438 India (Figs. 8f and 9f). Interestingly, the whole circulation pattern of regime #6 is very similar  
439 to the one obtained by reducing the albedo over Sahara and Pakistan arid regions in sensitivity  
440 coupled experiments (Sooraj et al. 2019).

441  
442 The four remaining ISMR regimes are all associated with strong rainfall anomalies (Fig. 7b-e),  
443 ENSO-like SST anomalies over the tropical Pacific (Fig. 8b-e) and significant modulations of  
444 the monsoon circulation in the Indian sector (Fig. 9b-e). Despite weaker tropical Pacific  
445 variability in mid- rather than late Holocene (Emile-Geay et al. 2016; White et al. 2018; Chen  
446 et al. 2019), tropical Pacific SST variability remains the main driver of ISMR variability during  
447 the mid-Holocene in our 5-simulation ensemble. Regimes #2 and #3 both represent ~15% of  
448 the classified patterns from 6 to 3.8 kyr BP (Table 3; 1<sup>st</sup> column). They describe significant wet  
449 anomalies over most or all India during La Niña-like conditions (Figs. 7b-c and 8b-c). These  
450 wet anomalies are due to moisture convergence favored by significant easterly wind anomalies  
451 over the western Pacific and eastern IO and an anticyclonic center over the Bay of Bengal (Fig.  
452 9b-c). However, regime #3 only is associated with a clear Gill-type response to convection and  
453 latent heat release over India, with strengthened 850-hPa southwesterlies over the Arabian Sea  
454 (Fig. 9c). On the other hand, regimes #4 and #5 (20% and 10% of the classified patterns,  
455 respectively: Table 3; 1<sup>st</sup> column) describe either widespread dryness or a north-south dipole  
456 over India under El Niño-like conditions (Figs. 7d-e and 8d-e). These abnormally dry conditions  
457 are systematically associated with 850-hPa westerly wind anomalies over the eastern IO–  
458 western Pacific (north of 10°N), reduced southwesterly monsoon fluxes over the Arabian Sea  
459 and a split of the monsoon trough over India (Fig. 9d-e), which is typical of drought conditions  
460 during the monsoon (Terray et al. 2005).

461  
462 Interestingly, the two ISMR regimes associated with widespread wet/dry rainfall anomalies of

463 same sign over all India (i.e., regimes #3 and #4: Fig. 7c-d) occur under well-defined ENSO-  
464 like – IOD collocation (Fig. 8c-d). Wet conditions over all India (Fig. 7c) are favored when  
465 these two coupled modes of variability collocate during their negative phases (i.e., La Niña-like  
466 and negative IOD: Fig. 8c). The reverse prevails for regime #4 (Figs. 7d and 8d). Regimes #3  
467 and #4 reflect the strong control of ENSO-like variability on both IOD and ISMR variability  
468 during mid-Holocene. This does not preclude positive/negative IODs to promote wet/dry ISMR  
469 at times, as suggested by e.g. Ashok et al. (2001 and 2004) but this is clearly not the dominant  
470 signal found here at the interannual-to-decadal timescale.

471

472 To verify whether or not these results are consistent with regimes obtained for modern ISMR  
473 variability, the clustering has been applied to the last 100 years of the TR5AS-Vlr01 and  
474 TR6AV-Sr02 ensemble (i.e., 1851-1950) and to 1901-2016 observations (CRU data for rainfall  
475 and HadISST data [Rayner et al. 2003] for SST). Despite the 6 ISMR regime patterns simulated  
476 for the last 100 years are not strictly similar to those derived from 6 to 3.8 kyr BP, the main  
477 modes affecting ISMR variability persist (Fig. 10). This demonstrates that ENSO remains the  
478 main driver of interannual-to-decadal ISMR variability for the last 6000 years regardless of the  
479 strength of orbital and trace gas forcing. The comparison with CRU-HadISST data reveals that  
480 the simulations reasonably represent the observed ISMR regimes and associated  
481 teleconnections, despite distorted ENSO patterns and exaggerated coupling with IO and  
482 Atlantic SST variability. The only exception concerns the wet ISMR regime associated to the  
483 strong IO basin-wide warming following strong El Niños (especially the 1982-83 and 1997/98)  
484 and the fast El Niño to La Niña transitions (Fig. 10), which represent the “best conditions” for  
485 a strong monsoon during recent decades (Boschat et al. 2011, 2012). The fact that this mode is  
486 not emerging in the simulations is probably linked to the inability of the model to produce a  
487 realistic negative IO feedback on ENSO, a bias shared by many current climate models,

488 especially those with a significant cold tongue bias in the equatorial Pacific like the IPSL model  
489 (Kug and Ham 2012; Li et al. 2019; Terray et al. 2020).

490

#### 491 4.2 Model version dependency

492

493 The model-version dependency of ISMR regimes is assessed in terms of anomalous rainfall  
494 patterns (Fig. 11) and total number of regime occurrence (Table 3). These analyses confirm that  
495 TR5AS-Vlr01 is an outlier, with largest departure from the ensemble mean (Fig. 11a) and  
496 underestimated occurrence of regimes #3 and #5 (Table 3). This suggests that ENSO and its  
497 teleconnection with ISMR and IO are much less diverse in this simulation compared to the  
498 others.

499

500 Overall, the ISMR regimes are very similar between the four TR6A simulations in terms of  
501 mean rainfall anomalies (Fig. 11b-e) and population (Table 3). We note, however, that the  
502 simulation set with fixed 1850 vegetation map (i.e., TR6AS-Sr10: Fig. 11b) deviates slightly  
503 more from the ensemble mean than those set with fixed mid-Holocene vegetation (i.e., TR6AS-  
504 Sr12: Fig. 11d) or dynamical vegetation (i.e., TR6AV-Sr02: Fig. 11e). Braconnot et al. (2019a)  
505 showed that bare soil and grass increase over India from mid- to late Holocene at the expense  
506 of forest (see their Fig. 10). Imposing more bare soil and grass and less forest over India during  
507 the mid-Holocene in TR6AS-Sr10 compared to TR6AS-Sr12 and TR6AV-Sr02 may thus affect  
508 vegetation-climate feedbacks through the modulation of albedo and local recycling.

509

#### 510 4.3 Evolution of the ISMR regimes and associated teleconnections

511

512 The frequency of occurrence of the ISMR regimes, computed every adjacent 100-yr windows,

513 is marked by stochastic centennial-to-multi-centennial fluctuations (Fig. 12). Cross-correlations  
514 between each ISMR regime are very noisy regardless of the metric. In particular, the frequency  
515 of occurrence of regime #3 is poorly correlated with that of regime #4 ( $r \sim |0.1|$  in most  
516 simulations). This indicates that centuries with changes in the occurrence of wet rainfall  
517 anomalies associated with La Niña-like – IOD- collocation are not necessarily accompanied by  
518 changes in the occurrence of dry anomalies associated to El Niño-like – IOD+ collocation.  
519 These results are consistent with the trends for ISMR wet and dry years displayed in Fig. 4d-e.  
520 We thus conclude that the relationship between ISMR and the two phases of ENSO-like – IOD  
521 is strongly skewed from 6 to 3.8 kyr BP at the centennial timescale.

522

523 On the other, none of the ISMR regimes depict a clear orbitally-driven trend from 6 to 3.8 kyr  
524 BP shared by the five simulations (Fig. 12). This contrasts with boreal summer SST variability  
525 in the Niño3.4, western tropical IO and eastern equatorial IO, which increases for the two  
526 former regions and decreases for the latter region in most simulations (Fig. 13a-c). The  
527 variability of the IOD, however, does not depict significant change (Fig. 13d) from 6 to 3.8 kyr  
528 BP. A first explanation of the absence of orbitally-driven changes in the ISMR regimes from 6  
529 to 3.8 kyr BP could involve interferences with low-frequency modes of internal variability.  
530 However, this hypothesis is rejected since the AHC procedure applied to 2-20-yr filtered  
531 rainfall anomalies leads to similar results. Another explanation could be that 6–3.8 kyr BP  
532 changes in ENSO-like variability may be too weak to influence ISMR regimes or, alternatively,  
533 that IOD variability may counteract ENSO's effects on ISMR, as suggested for the historical  
534 period (Ashok and Saji 2007).

535

536 When considering the last 6000 years, the ISMR regimes strongly connected to ENSO-like –  
537 IOD collocation become significantly more frequent from mid- to late Holocene in TR6AV-

538 Sr02 (Fig. 14). This trend concerns both wet and dry regimes associated to ENSO – IOD  
539 collocation in their negative and positive phases, respectively (Fig. 14), while only the dry  
540 regime associated to El Niño-like – IOD+ collocation in TR5AS-V1r01 (not shown). We thus  
541 make the hypothesis that the 6–3.8 kyr BP period is too short to detect changes in rainfall  
542 interannual-to-decadal variability, but that other variables could be better precursors of its long-  
543 term changes.

544

545 We thus examined changes in climate anomalies associated to the two ISMR regimes linked to  
546 ENSO – IOD collocation between the first and second half of the 6–3.8 kyr BP period (Fig.  
547 15). In both cases, we identified modest but significant changes in precipitable water over India  
548 linked to changes in both local evaporation and moisture advection from the western IO and  
549 southeast Asia. These changes are associated with strengthened tropical SST anomalies,  
550 particularly over the Pacific under El Niño conditions, suggesting increased control of ENSO  
551 on the Indian monsoon thermodynamics from 6 to 3.8 kyr BP. Precipitable water is thus a good  
552 precursor of changes in the interannual-to-decadal variability of the water cycle due to the  
553 Clausius-Clapeyron relationship. Rainfall appears to be the last link in the chain and is mediated  
554 by dynamic changes, which may have different and remote origins. This leads us to conclude  
555 that a threshold needs to be reached prior to see significant trends in rainfall interannual-to-  
556 decadal variability.

557

558

## 559 **5. Discussion and conclusion**

560

561 Results of the five transient simulations with the IPSL model show that the last 6000 years are  
562 marked by a significant drying trend in ISMR, consistent with previous studies (e.g., Bartlein

563 et al. 2011; Dallmeyer et al. 2015; Braconnot et al. 2019b). This drying trend affects the whole  
564 ISMR distribution, including the intensity and number of the 10% driest and 10% wettest  
565 seasons and is associated to a contraction of the ISMR season (Figs. 3-4). The magnitude of the  
566 drying trend is larger in simulations set with higher resolution and the new surface hydrology.  
567 Both the way runoff is routed to ocean and vegetation-climate feedbacks modulate the onset  
568 phase of the Indian monsoon (Fig. 3), but have modest effects at the seasonal timescale,  
569 including the time evolution of the number and intensity in flood and drought years (Fig. 4).

570

571 The interannual-to-decadal variability of JJAS rainfall significantly decreases over most of  
572 India from mid- to late Holocene but increases over central India and adjacent oceanic regions  
573 (Fig. 5). This variability is then decomposed into 6 physically consistent rainfall regimes to  
574 investigate changes in the ISMR teleconnections. From 6 to 3.8 kyr BP, the regimes are very  
575 similar between the 4 TR6A simulations but depict less diversity in the TR5A simulation (Table  
576 3). In all simulations, the two most energetic regimes in terms of rainfall intensity describe  
577 widespread dry/wet rainfall anomalies over India when ENSO and IOD collocate in their  
578 positive/negative phase (Figs. 7-8). This suggests that the ENSO forcing is dominant on both  
579 ISMR and IOD. The frequency of occurrence of these two ISMR regimes does not change from  
580 6 to 3.8 kyr BP (Fig. 12), contrary to the intensity of precipitable water (Fig. 15) identified here  
581 as a good parameter to detect emerging trends in monsoon variability. However, these two  
582 ISMR regimes become more frequent from 6 to 0 kyr BP (Fig. 14) as ENSO amplitude  
583 strengthens in our modeling framework (Fig. 6), consistent with increased ENSO variability as  
584 inferred by paleo reconstructions (Cobb et al. 2013; Carré et al. 2014; Emile-Geay et al. 2016).  
585 This suggests a reorganization of ISMR (and IOD) interannual-to-decadal variability from mid-  
586 to late Holocene, with increasing influence of ENSO and associated changes in the Walker  
587 circulation on both ISMR and IOD. On the other hand, the slow evolution of interannual-to-

588 decadal variability of JJAS Indian rainfall is never linked to IOD only in our modeling  
589 framework, consistent with ENSO-removed experiments (Crétat et al. 2017). This does not  
590 preclude the existence of IOD forcing on the Indian monsoon in some specific years or periods  
591 when ENSO is at rest. It would be worth to examine the ISMR–IOD relationship at different  
592 timescales and for different time slices with partially coupled simulations (e.g. without ENSO)  
593 to refine these results.

594

595 We also highlight that ISMR mean-state and interannual-to-decadal variability exhibit  
596 significant modulations at the multidecadal-to-multicentennial timescales that are not  
597 synchronous between the simulations (Figs. 4 and 12). This is consistent with previous  
598 modeling findings (e.g., Dalmeyer et al. 2015) and paleo reconstructions over India (Kathayat  
599 et al. 2016; Kaushal et al. 2018). Long-term droughts such as the multidecadal-to-centennial  
600 4.2 kyr BP event (Lézine et al. 2017; Yan and Liu 2019) may thus be caused by internal  
601 variability since solar cycles are not imposed in our simulations. Understanding their triggering  
602 mechanisms would lead to a strong improvement of ISMR predictability.

603

604 Finally, this study provides interesting tracks to model-data comparisons in the Indian sector.  
605 Mean-state and variability should be examined separately since their evolution can be opposite  
606 from mid- to late Holocene and their forcing mechanisms may differ. This also stands for the  
607 IO, which displays a positive-to-negative IOD-like SST mean-state, but increased (decreased)  
608 interannual-to-decadal variability in its western tropical (eastern equatorial) part from mid- to  
609 late Holocene (Fig. 6). Our results strongly suggest that this enhanced SST variability in the  
610 western IO is remotely forced by ENSO changes, independently of IOD or local mean-state  
611 changes. This complexity among timescales requires more investigations and may explain the  
612 disagreement among paleo-proxies for IOD evolution (Kwiatkowski et al. 2015 versus Abram



613 et al. 2007). Diagnosing changes or specific events in paleoclimate records remains, however,  
614 a great challenge since there is only a small probability for “big events” resulting from  
615 multiscale forcing and internal variability to be synchronous between paleo-reconstructions and  
616 simulations. Strategies based on analog are thus necessary to foster model-data comparisons  
617 and to utilize models for assessing the mechanisms driving such compound events.

## 618 **Appendix A: AHC procedure**

619

620 In this study, the AHC is adopted to identify recurrent ISMR regimes within our multi-  
621 configuration ensemble and analyze their temporal evolution primarily from 6 to 3.8 kyr BP  
622 but also from 6 to 0 kyr BP and for the 1851-1950 period. The AHC procedure consists in  
623 merging  $N$  anomalous JJAS rainfall patterns into  $N$ -to-1 clusters of size 1-to- $N$  according to  
624 their spatial similarity. The similarity between all pairs of patterns is measured using the  
625 Euclidean distance. Each pattern is merged with another according to the smallest pairwise  
626 Euclidean distance. The resulting merged cluster is then paired with another pattern or another  
627 cluster according to the Ward algorithm (Ward 1963), which minimizes intra-cluster variance  
628 and maximizes inter-cluster variance at each merging step. The procedure continues until all  
629 patterns are merged in a unique cluster. For a more detailed explanation of the AHC procedure  
630 we refer the reader to Cr  tat et al. (2019).

631

632 The AHC is applied to a time-space matrix constructed in three successive steps. Anomalous  
633 JJAS rainfall patterns are computed over India (i.e., 58 land points within 5  -25  N and 77  -  
634 88  E) for each simulation and each of the 22 100-yr windows from 6 to 3.8 kyr BP. For each  
635 100-yr window, the 100 anomalous rainfall patterns are defined as the departure from the  
636 corresponding 100-yr rainfall mean-state pattern. The anomalous rainfall patterns from the  
637 TR5AS-Vlr01 simulation are interpolated onto the horizontal resolution of the TR6A  
638 simulations (see Table 1) using a bilinear algorithm. The anomalous patterns from the five  
639 simulations are concatenated in a time-space matrix. A total of 10980 patterns are classified  
640 from 6 to 3.8 kyr BP instead of 11000 (2200 JJAS seasons x 5 simulations) because two  
641 simulations, TR6AS-Sr10 and TR6AS-Sr12, have 10 years missing due to technical issues with  
642 the data storage. The same methodology is applied from 6 to 0 kyr BP and for the 1851-1950

643 periods for the ensemble of the two 6000-yr simulations.

644

645 Figure A1 shows the dendrogram tree obtained at the end of the AHC procedure applied to the  
646 5-simulation ensemble from 6 to 3.8 kyr BP. The dendrogram summarizes all merging from  $N$   
647 to 1 clusters of size 1 to  $N$  (with  $N=10980$  being the total number of anomalous rainfall patterns  
648 feeding the AHC), as well as the evolution of the similarity metric for the last 10 merging. The  
649 evolution of the similarity metric indicates three main abrupt jumps: from 6 to 5 clusters, from  
650 3 to 2 clusters and from 2 to 1 clusters. A 2-cluster cutoff would mix ISMR regimes with  
651 opposite rainfall and SST anomalies (compare regimes #1 and #6 in Figs. 7-8). A 3-cluster  
652 cutoff would also mix very different regimes (compare regimes #1 with regimes #2-3 in Figs.  
653 7-8) and would merge regimes related to ENSO-like conditions with regimes related to ENSO-  
654 like – IOD collocation (compare regimes #2 and #3 and regimes #4 and #5 in Fig. 8). Here, we  
655 retain a 6-cluster cutoff to avoid such a mixing, which has no physical consistency, and because  
656 we aim at discussing internal variability and orbitally-forced evolution of only physically  
657 consistent regimes. This high-degree of refinement is required here since changes in ISMR  
658 variability remain subtle from mid- to late Holocene (Braconnot et al. 2019b).

659

660 The statistical robustness of a 6-regime cutoff is assessed by examining the spatial correlation  
661 between each anomalous rainfall pattern within a regime and its center of gravity defined as the  
662 ensemble mean anomalous rainfall pattern of the regime. When this spatial correlation is below  
663 0.2, the patterns are considered as outliers. The 0.2 threshold is deliberately low to avoid  
664 excluding patterns which are close to the center of gravity but slightly shifted in space. About  
665 20% of outliers are detected. They are almost equally distributed within the five simulations.  
666 These outliers are removed from all the analyses. Once the outliers removed, the 6 ISMR  
667 regimes synthesize 8963 patterns. The spatial correlation values obtained between each pattern

668 and its corresponding outlier-free center of gravity exceed +0.35 more than 75% of the time  
669 and the median correlation reaches at least +0.5 whatever the regime.

670 **Acknowledgments**

671

672 We acknowledge PRACE for awarding us access to Curie at GENCI@CEA, France (THROL  
673 project) to start the simulations. The simulations were also performed using HPC resources  
674 from GENCI-TGCC thanks to a high-end computing access grant and to our annual allocation  
675 time (gen2212). This work is supported by the JPI-Belmont PACMEDY project (ANR-15-  
676 JCLI-0003-01). It benefits from the development of the common modeling IPSL infrastructure  
677 coordinated by the IPSL climate modeling center (<https://cmc.ipsl.fr/>). We also acknowledge  
678 the three anonymous reviewers for their constructive comments.

679

680 **References**

681

682 Abram N, M Gagan, Z Liu, et al. (2007) Seasonal characteristics of the Indian Ocean Dipole  
683 during the Holocene epoch. *Nature* 445:299–302

684 Adler RF, et al. (2003) The Version 2 Global Precipitation Climatology Project (GPCP)  
685 Monthly Precipitation Analysis (1979 - Present). *J Hydrometeor* 4(6):1147–1167

686 Ashok K, Z Guan, T Yamagata (2001) Impact of the Indian Ocean dipole on the relationship  
687 between the Indian monsoon rainfall and ENSO. *Geophys Res Lett* 26:4499–4502

688 Ashok K, Z Guan, NH Saji, T Yamagata (2004) Individual and combined influences of ENSO  
689 and the Indian Ocean dipole on the Indian summer monsoon. *J Clim* 17:3141–3155

690 Ashok K, NH Saji (2007) On impacts of ENSO and Indian Ocean dipole events on the sub-  
691 regional Indian summer monsoon rainfall. *Nat Hazards* 42-2:273–285

692 Atsawawaranunt K, L Comas-Bru, S Amirnezhad Mozhdehi, et al. (2018) The SISAL database:  
693 a global resource to document oxygen and carbon isotope records from speleothems.  
694 *Earth Syst Sci Data* 10:1687–1713

695 Bartlein PJ, SP Harrison, S Brewer, et al. (2011) Pollen-based continental climate  
696 reconstructions at 6 and 21 ka: a global synthesis. *Clim Dyn* 37: 775–802

697 Bartlein PJ, SL Shafer (2019) Paleo calendar-effect adjustments in time-slice and transient  
698 climate-model simulations (PaleoCalAdjust v1.0): impact and strategies for data analysis.  
699 *Geosci Model Dev* 12:3889–3913

700 Behera SK, JJ Luo, S Masson, SA Rao, H Sakuma, T Yamagata (2006) A CGCM study on the  
701 interaction between IOD and ENSO. *J Clim* 19:1608–1705

702 Boschat G, P Terray, S Masson (2011) Interannual relationships between Indian summer  
703 monsoon and Indo-Pacific coupled modes of variability during recent decades. *Clim Dyn*  
704 37:1019–1043

705 Boschat G, P Terray, S Masson (2012) Robustness of SST teleconnections and precursory  
706 patterns associated with the Indian summer monsoon. *Clim Dyn* 38:2143–2165

707 Braconnot P, B Otto-Bliesner, SP Harrison, et al. (2007a) Results of PMIP2 coupled  
708 simulations of the Mid-Holocene and Last Glacial Maximum – Part 1: experiments and  
709 large-scale features. *Clim Past* 3:261–277

710 Braconnot P, B Otto-Bliesner, SP Harrison, et al. (2007b) Results of PMIP2 coupled  
711 simulations of the Mid-Holocene and Last Glacial Maximum – Part 2: feedbacks with  
712 emphasis on the location of the ITCZ and mid- and high latitudes heat budget. *Clim Past*  
713 3:279–296

714 Braconnot P, Y Luan, S Brewer, W Zheng (2012) Impact of Earth’s orbit and freshwater fluxes  
715 on Holocene climate mean seasonal cycle and ENSO characteristics. *Clim Dyn* 38:1081–  
716 1092

717 Braconnot P, D Zhu, O Marti, J Servonnat (2019a) Strengths and challenges for transient Mid-  
718 to Late Holocene simulations with dynamical vegetation. *Clim Past* 15:997–1024

719 Braconnot P, J Crétat, O Marti, et al. (2019b) Impact of Multiscale Variability on Last 6,000  
720 Years Indian and West African Monsoon Rain. *GRL*, doi:10.1029/2019GL084797

721 Carré M, JP Sachs, S Purca, et al. (2014) Holocene history of ENSO variance and asymmetry  
722 in the eastern tropical Pacific. *Science Rep*, doi:10.1126/science.1252220

723 Chen L, L Wang, T Li, J Liu (2019) Drivers of reduced ENSO variability in mid-Holocene in  
724 a coupled mode. *Clim Dyn* 52:5999–6014

725 Cobb KM, N Westphal, HR Sayani, et al. (2013) Highly variable El Niño-Southern Oscillation  
726 throughout the Holocene. *Science* 339:67–70

727 Crétat J, P Terray, S Masson, PV Sooraj, MK Roxy (2017) Indian Ocean and Indian Summer  
728 Monsoon : relationships without ENSO in ocean-atmosphere coupled simulations. *Clim*  
729 *Dyn* 49:1429–1448

730 Crétat J, P Terray, S Masson, KP Sooraj (2018) Intrinsic precursors and timescale of the tropical  
731 Indian Ocean Dipole: insights from partially decoupled numerical experiment. *Clim Dyn*  
732 51:1311–1332

733 Crétat J, B Pohl, B Dieppoiss, S Berthou, J Pergaud (2019) The Angola Low: relationship with  
734 southern African rainfall and ENSO. *Clim Dyn* 52:1783–1803

735 Dallmeyer A, M Claussen, N Fischer, et al. (2015) The evolution of sub-monsoon systems in  
736 the Afro-Asian monsoon region during the Holocene. *Clim Past* 11:305–326

737 Dallmeyer A, M Claussen, SJ Lorenz, T Shanahan (2019) The end of the African humid period  
738 as seen by a transient comprehensive Earth system model simulation of the last 8000  
739 years. *Clim Past*, doi:10.5194/cp-2019-86

740 Dufresne JL, MA Foujols, S Denvil, et al. (2013) Climate change projections using the IPSL-  
741 CM5 Earth System Model: from CMIP3 to CMIP5. *Clim Dyn* 40:2123–2165

742 Emile-Geay J, KM Cobb, M Carré, et al. (2015) Links between tropical Pacific seasonal,  
743 interannual and orbital variability during the Holocene. *Nature Geo*,  
744 doi:10.1038/NGEO2608

745 Enfield DB, AM Mestas-Nuñez, PJ Trimble (2001) The Atlantic Multidecadal Oscillation and  
746 its relation to rainfall and river flows in the continental US. *Geophys Res Lett* 28:2077–  
747 2080

748 Fischer N, JH Jungclaus (2011) Evolution of the seasonal temperature cycle in a transient  
749 Holocene simulation: orbital forcing and sea-ice. *Clim Past* 7:1139–1148

750 Gadgil S, PN Vinayachandran, PA Francis, S Gadgil (2004) Extremes of the Indian summer  
751 monsoon rainfall, ENSO and equatorial Indian Ocean oscillation. *Geophys Res Lett* 31,  
752 L12213, doi:10.1029/2004GL019733

753 Giesche A, M Staubwasser, CA Petrie, DA Hodell (2019) Indian winter and summer monsoon  
754 strength over the 4.2 ka BP event in foraminifer isotope records from the Indus River



755 delta in the Arabian Sea. *Clim Past* 15:73–90

756 Gong X, MB Richman (1995) On the application of cluster analysis to growing season  
757 precipitation data in North America East of the Rockies. *J Clim* 8:897–931

758 Goswami BB, BN Goswami (2017) A road map for improving dry-bias in simulating the South  
759 Asian monsoon precipitation by climate models. *Clim Dyn* 49:2025–2034

760 Harris I, PD Jones, TJ Osborn, DH Lister (2014) Updated high-resolution grids of monthly  
761 climatic observations – the CRU TS3.10 Dataset. *Int J Climatol* 34:623–642

762 Harrison SP, PJ Bartlein, K Izumi, et al. (2015) Evaluation of CMIP5 palaeo-simulations to  
763 improve climate projections. *Nature Clim Change* 5:735–743

764 Jalihal C, J Srinivasan, A Chakraborty (2019) Modulation of Indian monsoon by water vapor  
765 and cloud feedback over the past 22,000 years. *Nature Commun* 10, 5701,  
766 doi:10.1038/s41467-019-13754-6

767 Joshi MK, F Kucharski (2017) Impact of Interdecadal Pacific Oscillation on Indian summer  
768 monsoon rainfall: An assessment from CMIP5 climate models. *Clim Dyn* 48:2375–2391

769 Joussaume S, P Braconnot (1997) Sensitivity of paleoclimate simulation results to season  
770 definitions. *J Geophys Res* 102:1943-1956

771 Joussaume S, KE Taylor, P Braconnot, et al. (1999) Monsoon changes for 5000 years ago:  
772 Results of 18 simulations from the Paleoclimate Modeling Intercomparison Project  
773 (PMIP). *Geophys Res Lett* 26:859–862

774 Kageyama M, P Braconnot, L Bopp, et al. (2013a) Mid-Holocene and Last Glacial Maximum  
775 climate simulations with the IPSL model—part I: comparing IPSL\_CM5A to IPSL\_CM4.  
776 *Clim Dyn* 40:2447–2468

777 Kageyama M, P Braconnot, L Bopp, et al. (2013b) Mid-Holocene and last glacial maximum  
778 climate simulations with the IPSL model: part II: model-data comparisons. *Clim Dyn*  
779 40:2469–2495

780 Kathayat G, H Cheng, A Sinha, et al. (2016) Indian monsoon variability on millennial-orbital  
781 timescales. *Sci Rep* 6, 24374, doi:10.1038/srep24374

782 Kathayat G, H Cheng, A Sinha, et al. (2017) The Indian monsoon variability and civilization  
783 changes in the Indian subcontinent. *Science Adv* 3: e1701296

784 Kaushal N, SFM Breitenbach, FA Lechleitner, et al. (2018) The Indian Summer Monsoon from  
785 a Speleothem  $\delta^{18}\text{O}$  Perspective—A Review. *Quat* 29, doi:10.3390/quat1030029

786 Krishnamurthy L, Krishnamurthy V (2013) Influence of PDO on South Asian summer  
787 monsoon-ENSO relation. *Clim Dyn* 42:2397–2410

788 Krishnan R, M Sugi M (2003) Pacific decadal oscillation and variability of the Indian summer  
789 monsoon rainfall. *Clim Dyn* 21:233–242

790 Kug JS, Ham YG (2012) Indian Ocean feedback to the ENSO transition in a multi-model  
791 ensemble. *J Clim* 25:6942–6957

792

793 Kumar P, J Sanwal, AP Dimri, R Ramesh (2019) Contribution of diverse monsoon precipitation  
794 over Central and Northern India during mid to Late Holocene. *Quat Int* 507:217–223

795 Kutzbach JE (1981) Monsoon climate of the early Holocene: climate experiment with the  
796 Earth's orbital parameters for 9000 years ago. *Science* 214, 59–61; erratum 214, 606

797 Kwiatkowski C, M Prange, V Varma, S Steinke, D Hebbeln, M Mohtadi (2015) Holocene  
798 variations of thermocline conditions in the eastern tropical Indian Ocean. *Quat Sci Rev*  
799 114: 33–42

800 Lézine AM, SJ Ivory, P Braconnot, O Marti (2017) Timing of the southward retreat of the ITCZ  
801 at the end of the Holocene Humid Period in Southern Arabia: Data-model comparison.  
802 *Quat Sci Rev* 164:68–76

803 Li G, Y Jian, S Yang et al. (2019) Effect of excessive equatorial Pacific cold tongue bias on the  
804 El Niño-Northwest Pacific summer monsoon relationship in CMIP5 multi-model  
805 ensemble. *Clim Dyn* 52:6195–6212

806 Liu Z, Otto-Bliesner B, Kutzbach J, Li L, Shields C (2003) Coupled climate simulation of the  
807 evolution of global monsoons in the Holocene. *J Clim* 16:2472–2490

808 Liu Z, BL Otto-Bliesner, F He, et al. (2009) Transient Simulation of Last Deglaciation with a  
809 New Mechanism for Bølling-Allerød Warming. *Science* 325:310–314

810 Lorenz SJ, G Lohmann (2004) Acceleration technique for Milankovitch type forcing in a  
811 coupled atmosphere-ocean circulation model: method and application for the Holocene.  
812 *Clim Dyn* 23:727–743

813 Lorenz SJ, JH Kim, N Rimbu, RR Schneider, G Lohmann (2006) Orbitally driven insolation  
814 forcing on Holocene climate trends: Evidence from alkenone data and climate modeling.  
815 *Paleocean* 21, PA1002, doi:10.1029/2005PA001152

816 Madec G, R Bourdall\_e-Badie, P Bouttier, C Bricaud, D Bruciaferri, D Calvert, M  
817 Vancoppenolle (2017) NEMO ocean engine (version v3.6). Notes du Pôle de  
818 modélisation de l'Institut Pierre-Simon Laplace (IPSL). doi: 10.5281/zenodo.1472492

819 Malik A, Brönnimann S, Stickler A, Raible CC, Muthers S, Anet J, Rozanov E, Schmutz W  
820 (2017) Decadal to multidecadal scale variability of Indian summer monsoon rainfall in  
821 the Coupled Ocean-Atmosphere-Chemistry Climate Model SOCOL-MPIOM. *Clim Dyn*  
822 49:3551–3572

823 Malik A, S Brönnimann (2018) Factors affecting the inter-annual to centennial timescale  
824 variability of Indian summer monsoon rainfall. *Clim Dyn* 50:4347–4364

825 Mantua NJ, SR Hare, Y Zhang, JM Wallace, RC Francis (1997) A Pacific interdecadal climate  
826 oscillation with impacts on salmon production. *Bull Amer Meteor Soc* 78:1069-1079

827 Marti O, P Braconnot, JL Dufresne, et al. (2010) Key features of the IPSL ocean atmosphere  
828 model and its sensitivity to atmospheric resolution. *Clim Dyn* 34:1–26

829 Marzin C, P Braconnot (2009) Variations of Indian and African monsoons induced by  
830 insolation changes at 6 and 9.5 kyr BP. *Clim Dyn* 33:215-231

831 Otto-Bliesner BL, P Braconnot, SP Harrison, et al. (2016) The PMIP4 contribution to CMIP6  
832 - Part 2: Two Interglacials, Scientific Objective and Experimental Design for Holocene  
833 and Last Interglacial Simulations. *Geosci Model Dev Discuss* 1-36, doi:10.5194/gmd-  
834 2016-279

835 Parthasarathy B, AA Munot, DR Kothawale (1995) All India monthly and seasonal rainfall  
836 series: 1871–1993. *Theor Appl Climatol* 49:217–224

837 Philander SGH (1983) El Niño Southern Oscillation phenomena. *Nature*, 302:295–301

838 Prodhomme C, P Terray, S Masson, G Boschhat, T Izumo (2015) Oceanic factors controlling  
839 the Indian Summer Monsoon Onset in a coupled model. *Clim Dyn* 44: 977–1002

840 Kesava Rao AVR, SP Wani, K Srinivas (2020) Climate Change Impacts at Benchmark  
841 Watershed. In: Wani S., Raju K. (eds) *Community and Climate Resilience in the Semi-  
842 Arid Tropics*. Springer, Cham

843 Rasmusson EM, TH Carpenter (1983) The relationship between eastern equatorial Pacific sea  
844 surface temperatures and rainfall over India and Sri Lanka. *J Clim* 111:517–528

845 Rayner NA, DE Parker, EB Horton, et al. (2003) Global analyses of sea surface temperature,  
846 sea ice, and night marine air temperature since the late nineteenth century. *J Geophys Res*  
847 108, doi:10.1029/2002JD002670

848 Roxy MK, ST Chaithra (2018) Impacts of Climate Change on the Indian Summer Monsoon. In  
849 book: *Climate Change and Water Resources in India*. Publisher: Ministry of  
850 Environment, Forest and Climate Change (MoEF&CC), Government of India

851 Roy SS, GB Goodrich, RC Balling Jr (2003) Influence of El Niño/Southern oscillation, Pacific  
852 Decadal Oscillation, and local sea-surface temperature anomalies on peak season  
853 monsoon precipitation in India. *Clim Res* 25:171–178

854 Saji NH, BN Goswami, PN Vinayachandran, T Yamagata (1999) A dipole mode in the tropical  
855 Indian Ocean. *Nature*, 401:360–363

856 Sepulchre P, A Caubel, JB Ladant, et al. (2019) IPSL-CM5A2. An Earth System Model  
857 designed for multi-millennial climate simulations. *Geosci Model Dev Discuss*,  
858 doi:10.5194/gmd-2019-332

859 Shi J, Q Yan (2019) Evolution of the Asian–African Monsoonal Precipitation over the last 21  
860 kyr and the Associated Dynamic Mechanisms. *J Clim*, doi:10.1175/JCLI-D-19-0074.1

861 Sikka DR (1980) Some aspects of the large-scale fluctuations of summer monsoon rainfall over  
862 India in relation to fluctuations in the planetary and regional scale circulation parameters.  
863 *Proc Indian Acad Sci Earth Planet Sci* 89:179–195

864 Sooraj KP, P Terray, S Masson, J Crétat (2019) Modulations of the Indian summer monsoon  
865 by the hot subtropical deserts: insights from sensitivity experiments. *Clim Dyn* 52:4527–  
866 4555

867 Sperber KR, H Annamalai, IS Kang, A Kitoh, A Moise, A Turner, B Wang, T Zhou (2013) The  
868 Asian summer monsoon: an intercomparison of CMIP5 vs. CMIP3 simulations of the late  
869 20th century. *Clim Dyn* 41:2711–2744

870 Staubwasser M, F Sirocko, PM Grootes, M Segl (2003) Climate change at the 4.2 ka BP  
871 termination of the Indus valley civilization and Holocene south Asian monsoon  
872 variability. *Geophys Res Lett* 30, doi:10.1029/2002GL016822

873 Terray P, E Guilyardi, AS Fischer, P Delecluse (2005) Dynamics of Indian Monsoon and ENSO  
874 Relationships in the SINTEX global Coupled Model. *Clim Dyn* 24: 145–168

875 Terray P, KP Sooraj, S Masson, RPM Krishna, G Samson and AG Prajeesh (2018) Towards a  
876 realistic simulation of boreal summer tropical rainfall climatology in state-of-the art  
877 coupled models: role of the background snow-free albedo. *Clim Dyn* 50:3413–3439

878 Terray P, KP Sooraj, S Masson, C Prodhomme (2020) Anatomy of the Indian Summer  
879 Monsoon and ENSO relationships in state-of-the-art CGCMs: Role of the tropical Indian  
880 Ocean. Submitted to *Clim Dyn*

881 Varma V, M Prange, U Merkel, T Kleinen, G Lohmann, M Pfeiffer, H Renssen, A Wagner, S  
882 Wagner, M Schulz (2012) Holocene evolution of the Southern Hemisphere westerly  
883 winds in transient simulations with global climate models. *Clim Past* 8:391–402

884 Varma V, M Prange, M Schulz (2016) Transient simulations of the present and the last  
885 interglacial climate using the Community Climate System Model version 3: effects of  
886 orbital acceleration. *Geosci Model Dev* 9:3859–3873

887 Walker GT (1924) Correlations in seasonal variations of weather. I. A further study of world  
888 weather. *Mem Indian Meteorol Dep* 24:275–332

889 Wang B, QH Ding, XH Fu, IS Kang, K Jin, J Shukla, F Doblas-Reyes (2005) Fundamental  
890 challenge in simulation and prediction of summer monsoon rainfall. *Geophys Res Lett*  
891 32, L15711, doi:10.1029/2005GL022734

892 Ward JH (1963) Hierarchical grouping to optimize an objective function. *J Am Stat Assoc*  
893 58:236–244

894 White SM, AC Ravelo, PJ Polissa (2018) Dampened El Niño in the Early and Mid-Holocene  
895 Due To Insolation-Forced Warming/Deepening of the Thermocline. *Geophys Res Lett* 45,  
896 doi:10.1002/2017GL075433

897 Yan M, J Liu (2019) Physical processes of cooling and mega-drought during the 4.2 ka BP  
898 event: results from TraCE-21ka simulations. *Clim Past* 15:265–277

899 Zhao Y, P Braconnot, O Marti, et al. (2005) A Multi-model analysis of the role of the ocean on  
900 the African and Indian monsoon during the mid-Holocene. *Clim Dyn* 25:777–800

901 Zhao Y, SP Harrison (2012) Mid-Holocene monsoons: a multi-model analysis of the inter-  
902 hemispheric differences in the responses to orbital forcing and ocean feedbacks. *Clim*  
903 *Dyn* 39:1457–1487

904

905 **Table Captions**

906

907

908 **Table 1:** Major differences in model set up between the five simulations analyzed in this study.

909 All simulations have the ORCA 2° ocean grid with 31 vertical levels. The LR and MR

910 resolutions stand for the atmospheric horizontal resolution. The LR (MR) atmosphere

911 resolution is 3.75° (2.5°) in longitude and 1.875° (1.25°) in latitude with 39 vertical levels in

912 both LR and MR. See main text for the description of the model version, the land surface, the

913 land-ocean river runoff and the experimental design for prescribing or computing vegetation.

914

915 **Table 2:** Mean-state and variability of July-to-September seasonal ISMR (land points in the

916 5°-25°N – 77°-88°E region) for the 1871-2012 AIR, 1979-2010 GPCP and 1901-2016 CRU

917 data and for the last 100 years of the two simulations (1851-1950). Variability is computed as

918 the standard-deviation of JJAS rainfall anomalies. Values in parenthesis correspond to the

919 standard-deviation of the results obtained for the 123, 97 and 81 20-yr windows of the AIR,

920 CRU and two simulations.

921

922 **Table 3:** Number of patterns (and percentage) within each of the six ISMR regimes after

923 removing the outliers. The percentage in the first column is expressed against the total number

924 of classified patterns. The percentage in the remaining columns corresponds to the weight each

925 simulation has on the total number of patterns spent in each ISMR regime (given in the first

926 column).

927

928 **Figure Captions**

929

930 **Figure 1:** (a) Mean seasonal cycle of monthly rainfall area-averaged over India (land points  
931 within the 5°-25°N – 70°-88°E region) for the 1871-2012 AIR and 1901-2016 CRU and 1979-  
932 2010 GPCP data, and the last 100 years of the TR5AS-Vlr01 and TR6AV-Sr02 simulations  
933 (i.e., 1851-1950). For the AIR data and the two simulations, thin curves show sampling errors  
934 defined as the mean seasonal cycle of all possible 20-yr windows along the 1871-2012 and  
935 1851-1950 period, respectively. (b) Same as (a) but for Indian rainfall variability defined as the  
936 standard-deviation of rainfall anomalies.

937

938 **Figure 2:** Location of the 2 mm/day isohyet from April to September for the (a) 1979-2010  
939 GPCP and (b) 1901-2016 CRU data and the last 100 years (i.e., 1851-1950) of the (c) TR5AS-  
940 Vlr01 and (d) TR6AV-Sr02 simulations.

941

942 **Figure 3:** Mid- to late Holocene changes in the (a-b) mean-state and (c-d) variability of rainfall  
943 area-averaged over India for the TR5AS-Vlr01 and TR6AV-Sr02 simulations. Both mean-state  
944 and variability are computed along 100-yr adjacent windows. (e-h) Relative differences in  
945 rainfall mean-state between the four TR6 simulations and their ensemble mean for each 100-yr  
946 adjacent from 6 to 3.8 kyr BP.

947

948 **Figure 4:** (a-b) PDF of JJAS rainfall area-averaged over India computed along each 100-yr  
949 adjacent window for the TR5AS-Vlr01 and TR6AV-Sr02 simulations, respectively. Blue-to-  
950 red colors show the evolution of the PDFs from mid- to late Holocene. (c) Evolution of the 10<sup>th</sup>  
951 and 90<sup>th</sup> percentile threshold values of ISMR anomalies for the five simulations. The percentile  
952 threshold values for each simulation are computed along each 100-yr moving window with 1-  
953 year increment between each window, giving one value for each year, and are displayed as  
954 ISMR departures from the first 100-yr climatology to remove offset differences between the  
955 simulations induced by different initial conditions. (d-e) Evolution in the number of the 10%  
956 driest and 10% wettest ISMR seasons in each simulation defined using the 10<sup>th</sup> and 90<sup>th</sup>  
957 percentile threshold values from the first 100-yr window.

958

959 **Figure 5:** Snapshots of mid- to late Holocene significant changes in JJAS rainfall mean-state  
960 (dashed/solid contours for |0.2|, |1.5| and |3| mm/day dry/wet differences) and standard-  
961 deviation (shadings) for the TR6AV-Sr02 simulation. For each 100-yr adjacent window,



962 changes in mean-state and standard-deviation are computed as the departure from the first 100  
963 years of the simulation (e.g. 6-5.9 kyr BP period) and significance is tested at the 95%  
964 confidence level according to a Student t test and a Chi-square test, respectively. (a) Mean and  
965 standard-deviation changes (averages on 4 100-yr adjacent windows) from 5.9 to 5.5 kyr BP  
966 that reach the 95% confidence level in at least 2 100-yr windows. (b-f) Same as (a) but for  
967 changes averaged on 5 100-yr consecutive windows from 5 to 4.5, 4 to 3.5, 3 to 2.5, 2 to 1.5  
968 and 1 to 0.5 kyr BP time interval, respectively, that reach the 95% confidence level in at least  
969 3 100-yr windows in the time interval.

970

971 **Figure 6:** Same as Fig. 5 but for changes in SST mean-state (dashed/solid contours for  $|0.1|$ ,  
972  $|0.4|$  and  $|1|$ °C cold/warm differences) and standard-deviation (shadings).

973

974 **Figure 7:** (a) Ensemble mean anomalous rainfall pattern associated to ISMR regime #1. Only  
975 rainfall anomalies that are significant at the 95% confidence level according to a Student t test  
976 are shown. (c-f) Same as (a) but for the 5 remaining ISMR regimes.

977

978 **Figure 8:** Same as Fig. 8 but for SST anomalies (°C), except significant SST anomalies are  
979 contoured in black.

980

981 **Figure 9:** Same as Fig. 8 but for 850-hPa wind anomalies (vectors; m/s) and associated  
982 divergence (shadings; m/s; blue = anomalous convergence; red = anomalous divergence). Wind  
983 anomalies are shown in black when at least one component (i.e., zonal or meridian) depict  
984 significant changes tested as in Fig. 8.

985

986 **Figure 10:** (a) Ensemble mean rainfall and SST anomalies associated with the six ISMR  
987 regimes identified by applying the AHC clustering to the last 100 years (i.e., 1851-1950) of the  
988 TR5AS-Vlr01 and TR6AV-Sr02 ensemble. Significant anomalies at the 95% confidence level  
989 according to a Student t test are contoured in black. (b) Same as (a) but for the CRU-HadISST  
990 data for the 1901-2016 period.

991

992 **Figure 11:** Model dependency in the mean anomalous rainfall pattern associated to the six  
993 ISMR regimes for (a-e) the five simulations. For each ISMR regime, model dependency is  
994 defined as the departure of the mean anomalous rainfall pattern of each simulation from the  
995 ensemble mean anomalous rainfall pattern shown in Fig. 8. Only departure significant at the

996 95% confidence level according to a Student t test is shown.

997

998 **Figure 12:** (a-f) Century-to-century evolution in the frequency of occurrence of the six ISMR  
999 regimes from 6 to 3.8 kyr BP for the five simulations. The frequency of occurrence is displayed  
1000 as the departure from its mean value.

1001

1002 **Figure 13:** Century-to-century evolution in boreal summer (JJAS) SST variability of the (a)  
1003 Niño3.4, (b) western tropical IO (10°S-10°N; 50°-70°E), (c) eastern equatorial IO (10°S-Eq;  
1004 90°-110°E) and (d) IOD indices from 6 to 3.8 kyr BP for the five simulations. Variability is  
1005 defined as standard-deviation of SST anomalies for each 100-yr adjacent window. The  
1006 variability is displayed as the departure from the mean value of the standard-deviations  
1007 computed for each 100-yr adjacent window.

1008

1009 **Figure 14:** (a; upper panel) Century-to-century evolution in the frequency of occurrence of the  
1010 ISMR regime associated to La Niña-like – IOD- collocation from 6 to 0 kyr BP for the TR6AV-  
1011 Sr02 simulation. This ISMR regime is extracted by applying the AHC clustering to anomalous  
1012 Indian rainfall patterns from 6 to 0 kyr BP in the two 6000-yr simulation ensemble (TR5AS-  
1013 Vlr01 and TR6AV-Sr02) with a 6-regime cutoff. The frequency of occurrence is expressed as  
1014 the departure from its mean value. (a; bottom panels) Number of occurrences of this ISMR  
1015 regime along each 2000-yr adjacent window and associated mean anomalous SST patterns.  
1016 Only SST anomalies significant at the 95% confidence level according to a Student t test are  
1017 shown. (b) Same as (a) but for the ISMR regime associated to El Niño-like – IOD+ collocation.

1018

1019 **Figure 15:** (a) 4.9-3.8 minus 6-4.9 kyr BP differences in precipitable water, SST, moisture  
1020 transport and evaporation ensemble mean anomalies associated to regime #3. Significant  
1021 anomalies at the 95% confidence level according to a Student two-tailed t test are contoured in  
1022 black for precipitable water, SST and evaporation and shown with black vectors for moisture  
1023 transport. (b) Same as (a) but for regime #4.

1024

1025 **Figure A1:** (a) Dendrogram tree obtained at the end of the AHC procedure applied to JJAS  
1026 rainfall anomalies simulated over India by the 5-simulation ensemble from 6 to 3.8 kyr BP. (b)  
1027 Evolution of the similarity metric for the 10 last mergings. See Appendix A for details.

1028

1029 **Tables**

1030

Simulation	Model version	Resolution	Land-surface	Dynamical vegetation	Land-ocean river runoff	Integration length
TR5AS-Vlr01	TR5A	LR	CM5	No – present	CM6	6,000 years
TR6AV-Sr02	TR6A	MR	11 layers	Yes	Inter	6,000 years
TR6AS-Sr10	TR6A	MR	11 layers	No – present	Inter	4,000 years
TR6AS-Sr11	TR6A	MR	11 layers	No – present	CM6	2,250 years
TR6AS-Sr12	TR6A	MR	11 layers	No – Mid-Holocene	Inter	2,250 years

1031

1032

1033

1034

1035

1036

1037

1038

**Table 1:** Major differences in model set up between the five simulations analyzed in this study. All simulations have the ORCA 2° ocean grid with 31 vertical levels. The LR and MR resolutions stand for the atmospheric horizontal resolution. The LR (MR) atmosphere resolution is 3.75° (2.5°) in longitude and 1.875° (1.25°) in latitude with 39 vertical levels in both LR and MR. See main text for the description of the model version, the land surface, the land-ocean river runoff and the experimental design for prescribing or computing vegetation.

	Mean State (mm.day <sup>-1</sup> )	Variability (mm.day <sup>-1</sup> )
AIR	6.93 (+/- 0.15)	1.22 (+/- 0.13)
GPCP	7.36	1.13
CRU	6.73 (+/- 0.15)	1.33 (+/- 0.10)
Vlr01	4.84 (+/- 0.18)	1.05 (+/- 0.11)
Sr02	5.72 (+/- 0.15)	1.34 (+/- 0.13)

1039  
1040  
1041  
1042  
1043  
1044  
1045  
1046

**Table 2:** Mean-state and variability of July-to-September seasonal ISMR (land points in the 5°-25°N – 77°-88°E region) for the 1871-2012 AIR, 1979-2010 GPCP and 1901-2016 CRU data and for the last 100 years of the two simulations (1851-1950). Variability is computed as the standard-deviation of JJAS rainfall anomalies. Values in parenthesis correspond to the standard-deviation of the results obtained for the 123, 97 and 81 20-yr windows of the AIR, CRU and two simulations.

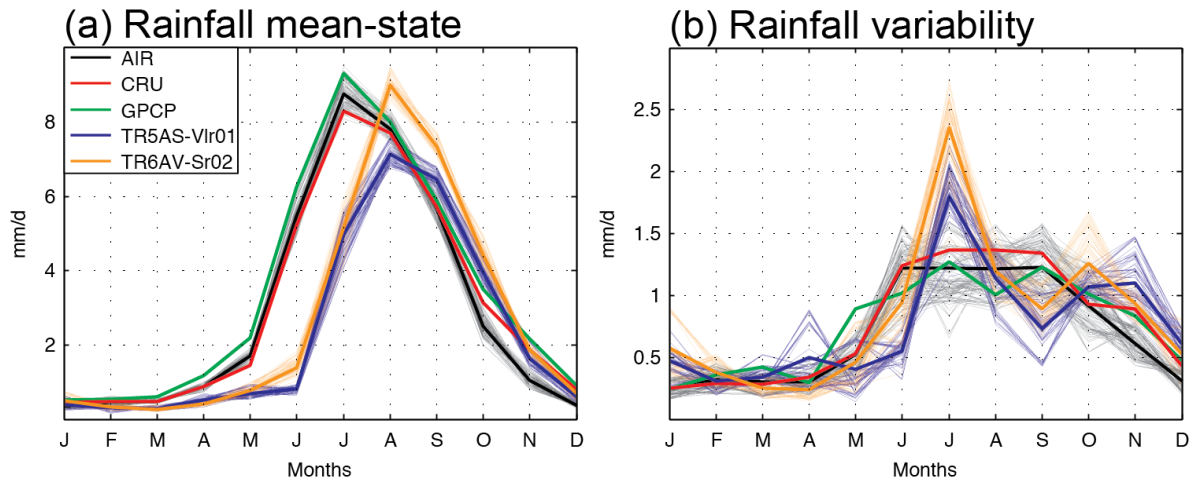
	Total	TR5AS- Vlr01	TR6AS- Sr10	TR6AS- Sr11	TR6AS- Sr12	TR6AV- Sr02
CL#1	1227 (13.7%)	333 (27.1)	199 (16.2)	221 (18)	238 (19.4)	236 (19.2)
CL#2	1344 (15%)	425 (31.6)	229 (17)	229 (17)	237 (17.6)	224 (16.7)
CL#3	1278 (14.2%)	131 (10.3)	280 (21.9)	292 (22.8)	296 (23.2)	279 (21.8)
CL#4	1821 (20.3%)	477 (26.2)	345 (18.9)	344 (18.9)	328 (18)	327 (18)
CL#5	933 (10.4%)	39 (4.2)	252 (27)	222 (23.8)	209 (22.4)	211 (22.6)
CL#6	2360 (26.3%)	288 (12.2)	489 (20.7)	518 (21.9)	521 (22.1)	544 (23.1)
Total	8963	1693	1794	1826	1829	1821

1048  
1049  
1050  
1051  
1052  
1053  
1054

**Table 3:** Number of patterns (and percentage) within each of the 6 recurrent ISMR regimes after removing the outliers. The percentage in the first column is expressed against the total number of classified patterns. The percentage in the remaining columns corresponds to the weight each simulation has on the total number of patterns spent in each ISMR regime (given in the first column).

1055 **Figures**

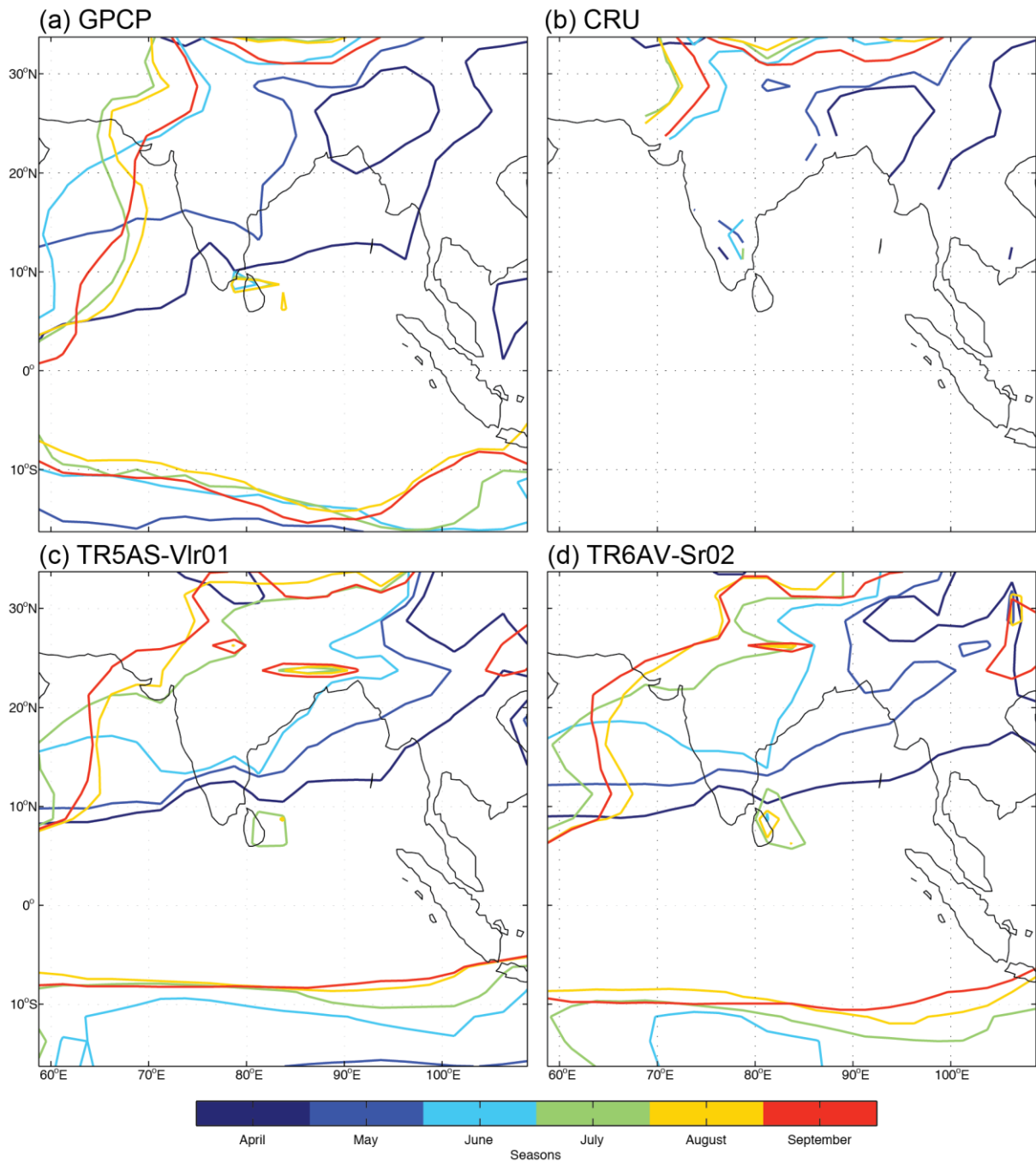
1056



1057

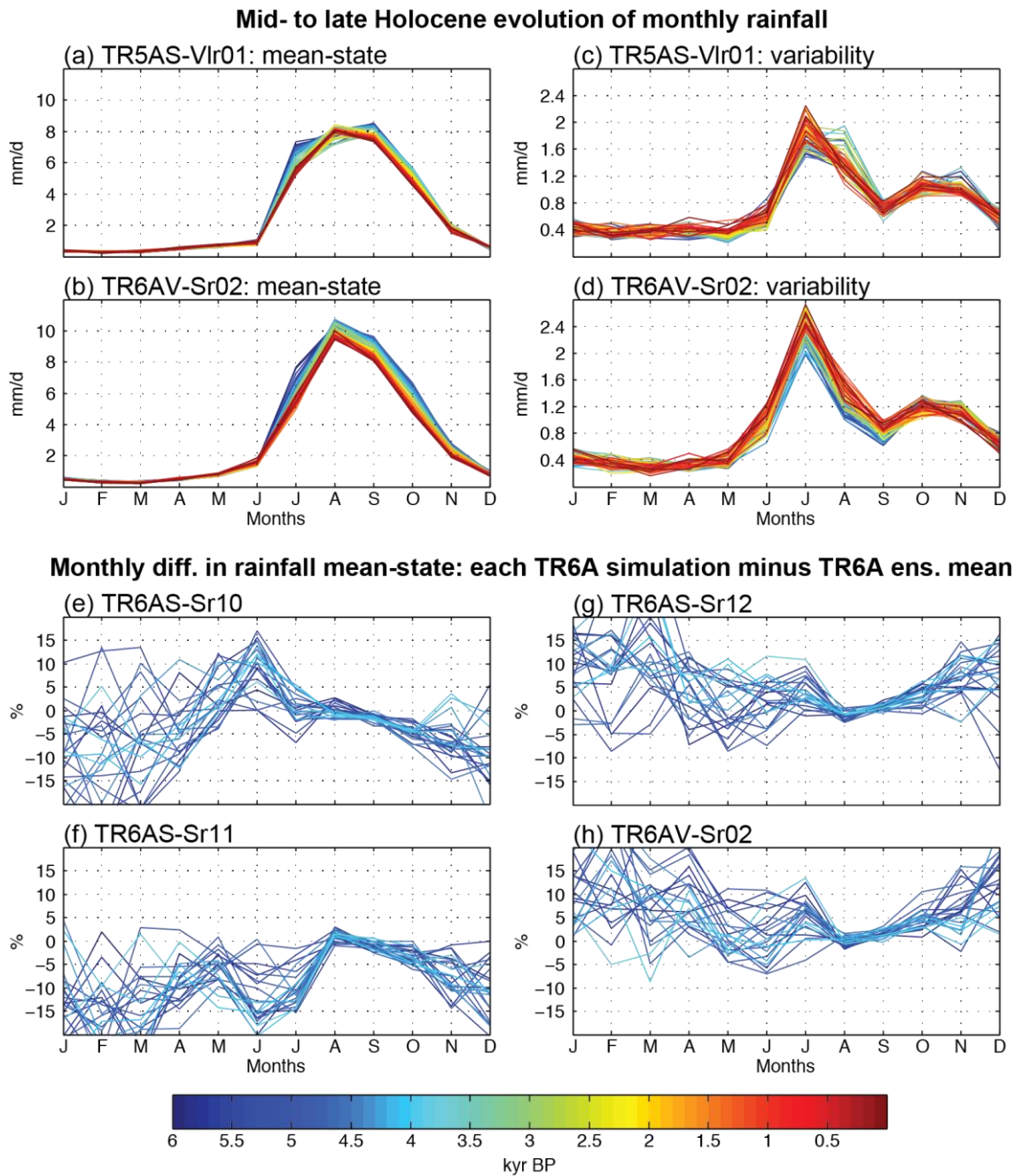
1058

1059 **Figure 1:** (a) Mean seasonal cycle of monthly rainfall area-averaged over India (land points  
1060 within the 5°-25°N – 70°-88°E region) for the 1871-2012 AIR and 1901-2016 CRU and 1979-  
1061 2010 GPCP data, and the last 100 years of the TR5AS-Vlr01 and TR6AV-Sr02 simulations  
1062 (i.e., 1851-1950). For the AIR data and the two simulations, thin curves show sampling errors  
1063 defined as the mean seasonal cycle of all possible 20-yr windows along the 1871-2012 and  
1064 1851-1950 period, respectively. (b) Same as (a) but for Indian rainfall variability defined as the  
1065 standard-deviation of rainfall anomalies.  
1066



1067  
 1068  
 1069  
 1070  
 1071  
 1072

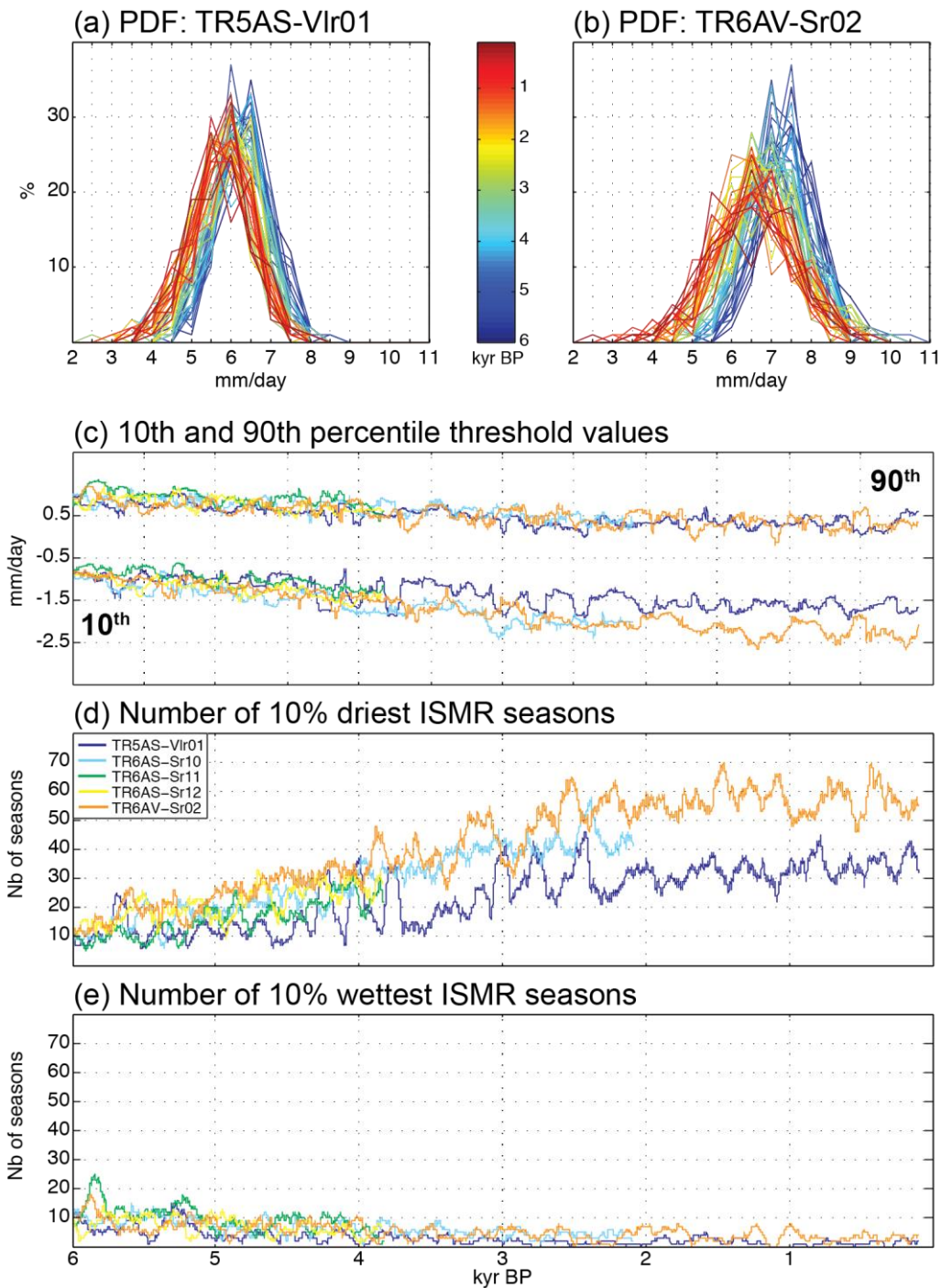
**Figure 2:** Location of the 2 mm/day isohyet from April to September for the (a) 1979-2010 GPCP and (b) 1901-2016 CRU data and the last 100 years (i.e., 1851-1950) of the (c) TR5AS-Vlr01 and (d) TR6AV-Sr02 simulations.



1073  
1074  
1075  
1076  
1077  
1078  
1079

**Figure 3:** Mid- to late Holocene changes in the (a-b) mean-state and (c-d) variability of rainfall area-averaged over India for the TR5AS-Vlr01 and TR6AV-Sr02 simulations. Both mean-state and variability are computed along 100-yr adjacent windows. (e-h) Relative differences in rainfall mean-state between the four TR6 simulations and their ensemble mean for each 100-yr adjacent from 6 to 3.8 kyr BP.

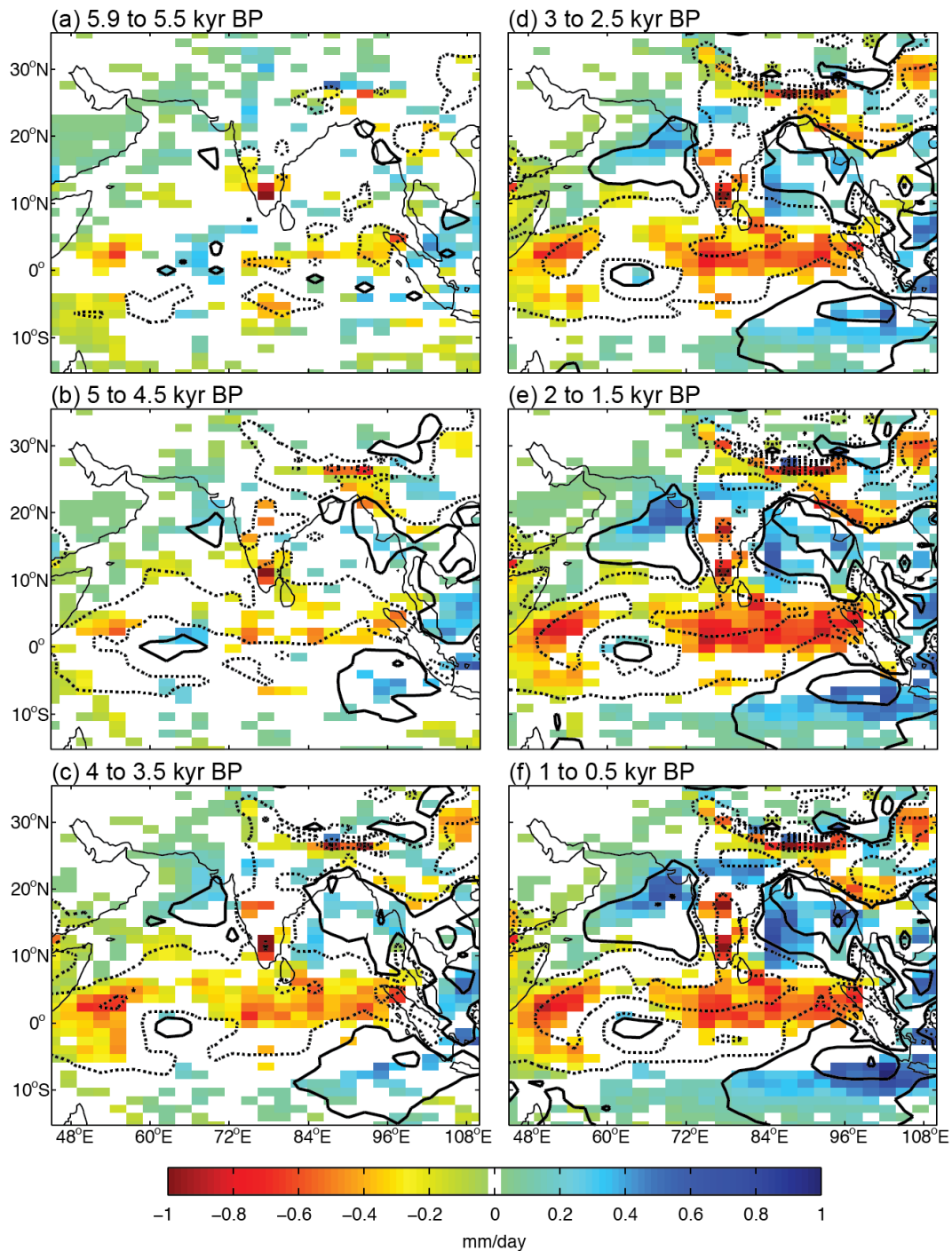




1080

1081

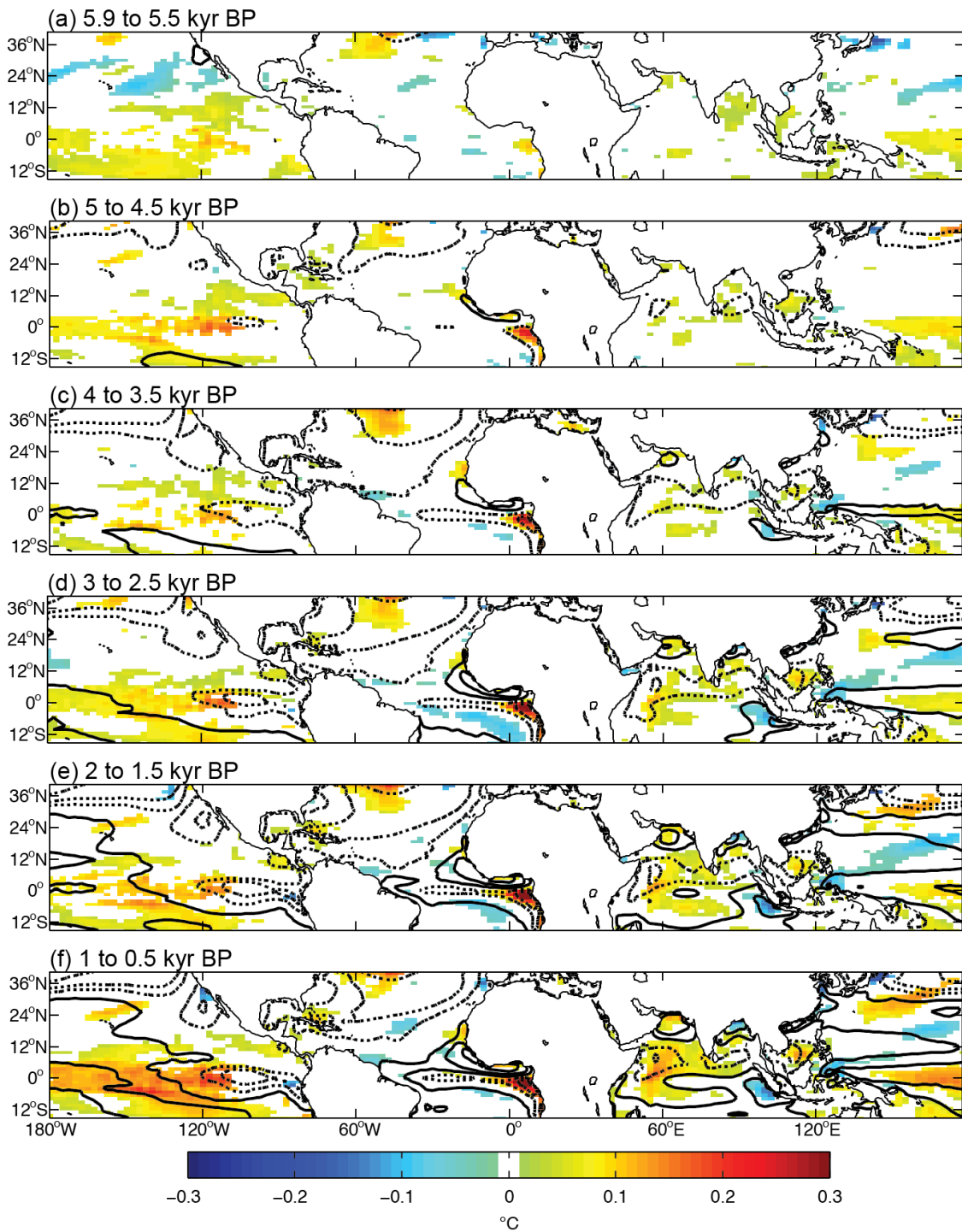
1082 **Figure 4:** (a-b) PDF of JJAS rainfall area-averaged over India computed along each 100-yr  
 1083 adjacent window for the TR5AS-Vlr01 and TR6AV-Sr02 simulations, respectively. Blue-to-  
 1084 red colors show the evolution of the PDFs from mid- to late Holocene. (c) Evolution of the 10<sup>th</sup>  
 1085 and 90<sup>th</sup> percentile threshold values of ISMR anomalies for the five simulations. The percentile  
 1086 threshold values for each simulation are computed along each 100-yr moving window with 1-  
 1087 year increment between each window, giving one value for each year, and are displayed as  
 1088 ISMR departures from the first 100-yr climatology to remove offset differences between the  
 1089 simulations induced by different initial conditions. (d-e) Evolution in the number of the 10%  
 1090 driest and 10% wettest ISMR seasons in each simulation defined using the 10<sup>th</sup> and 90<sup>th</sup>  
 1091 percentile threshold values from the first 100-yr window.



1092

1093

1094 **Figure 5:** Snapshots of mid- to late Holocene significant changes in JJAS rainfall mean-state  
 1095 (dashed/solid contours for  $|0.2|$ ,  $|1.5|$  and  $|3|$  mm/day dry/wet differences) and standard-  
 1096 deviation (shadings) for the TR6AV-Sr02 simulation. For each 100-yr adjacent window,  
 1097 changes in mean-state and standard-deviation are computed as the departure from the first 100  
 1098 years of the simulation (e.g. 6-5.9 kyr BP period) and significance is tested at the 95%  
 1099 confidence level according to a Student t test and a Chi-square test, respectively. (a) Mean and  
 1100 standard-deviation changes (averages on 4 100-yr adjacent windows) from 5.9 to 5.5 kyr BP  
 1101 that reach the 95% confidence level in at least 2 100-yr windows. (b-f) Same as (a) but for  
 1102 changes averaged on 5 100-yr consecutive windows from 5 to 4.5, 4 to 3.5, 3 to 2.5, 2 to 1.5  
 1103 and 1 to 0.5 kyr BP time interval, respectively, that reach the 95% confidence level in at least  
 1104 3 100-yr windows in the time interval.

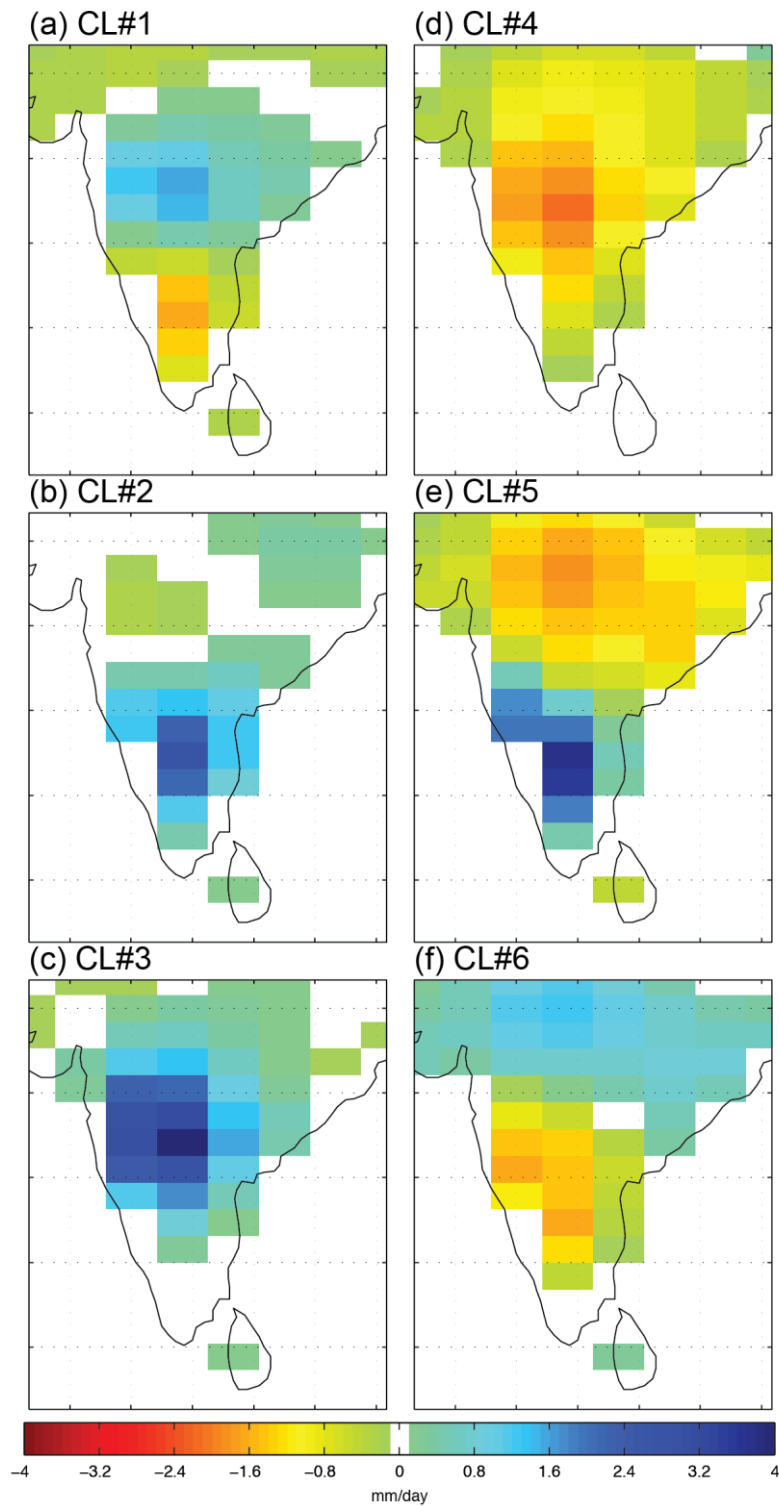


1105

1106

1107 **Figure 6:** Same as Fig. 5 but for changes in SST mean-state (dashed/solid contours for  $|0.1|$ ,

1108  $|0.4|$  and  $|1|$ °C cold/warm differences) and standard-deviation (shadings).

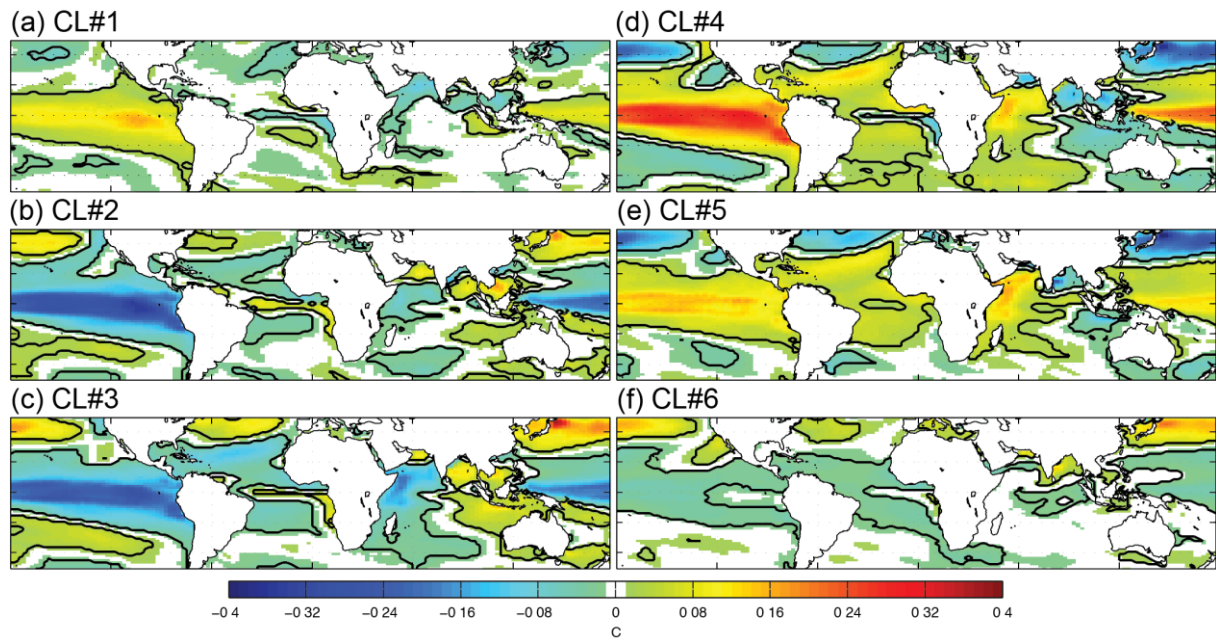


1109

1110

1111 **Figure 7:** (a) Ensemble mean anomalous rainfall pattern associated to ISMR regime #1. Only  
 1112 rainfall anomalies that are significant at the 95% confidence level according to a Student t test  
 1113 are shown. (c-f) Same as (a) but for the 5 remaining ISMR regimes.

1114

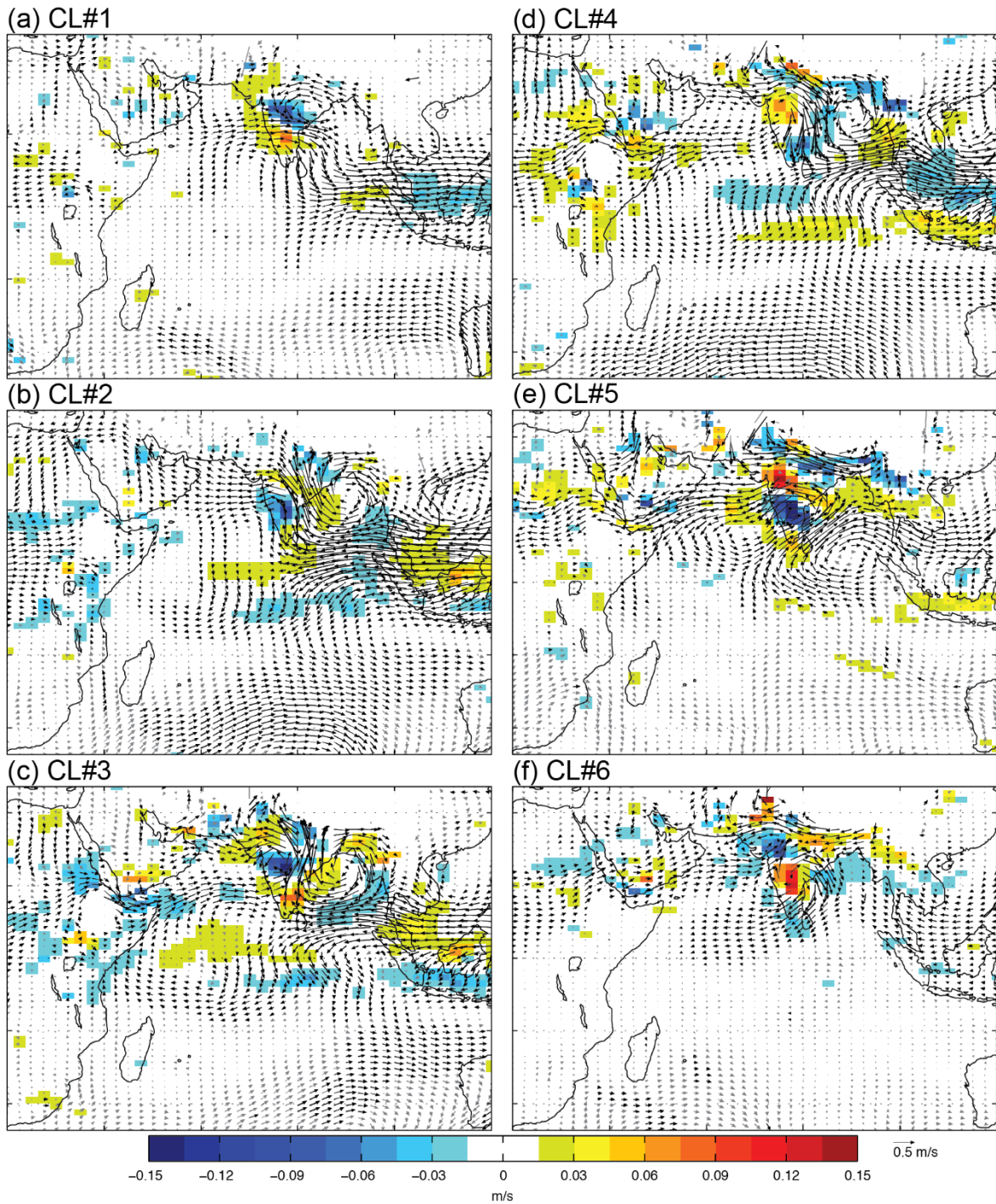


1115

1116

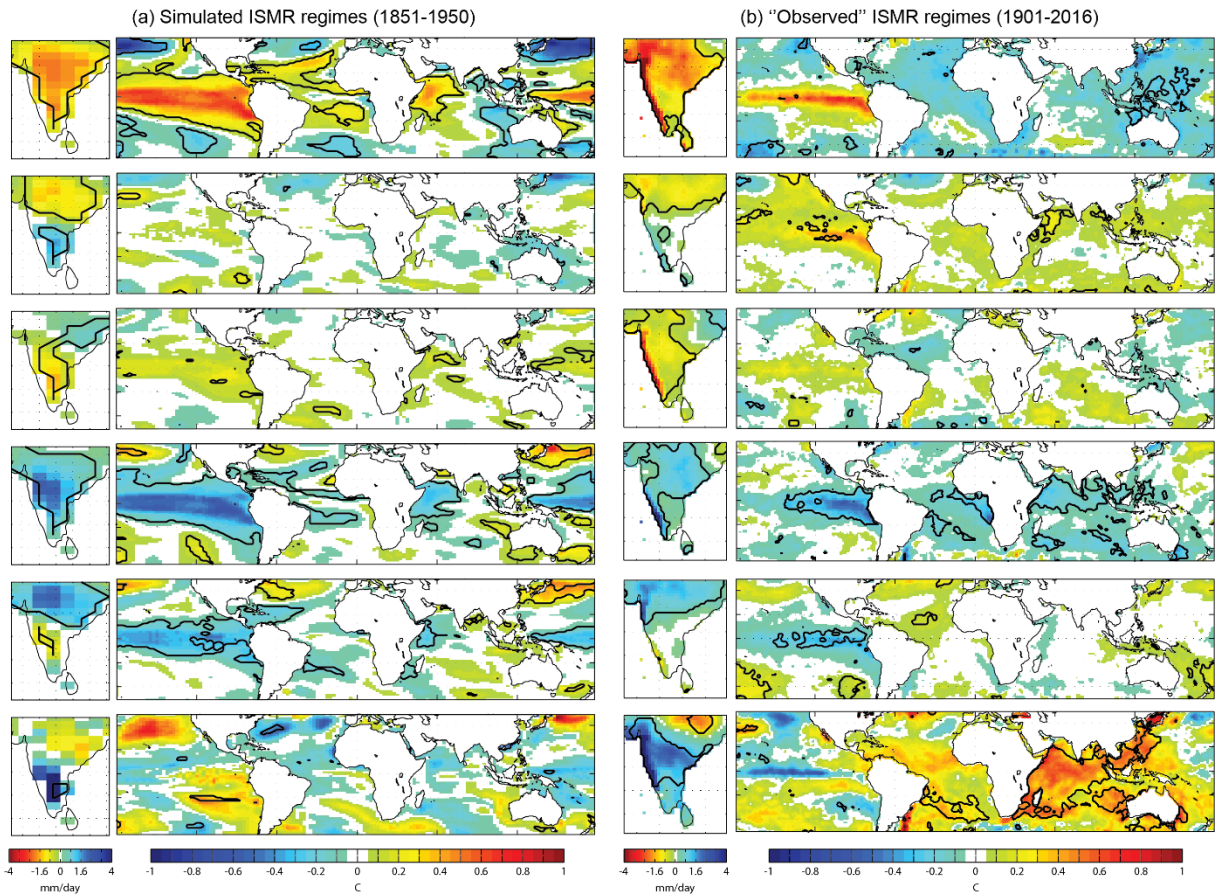
1117 **Figure 8:** Same as Fig. 7 but for SST anomalies ( $^{\circ}\text{C}$ ), except significant SST anomalies are  
 1118 contoured in black.

1119



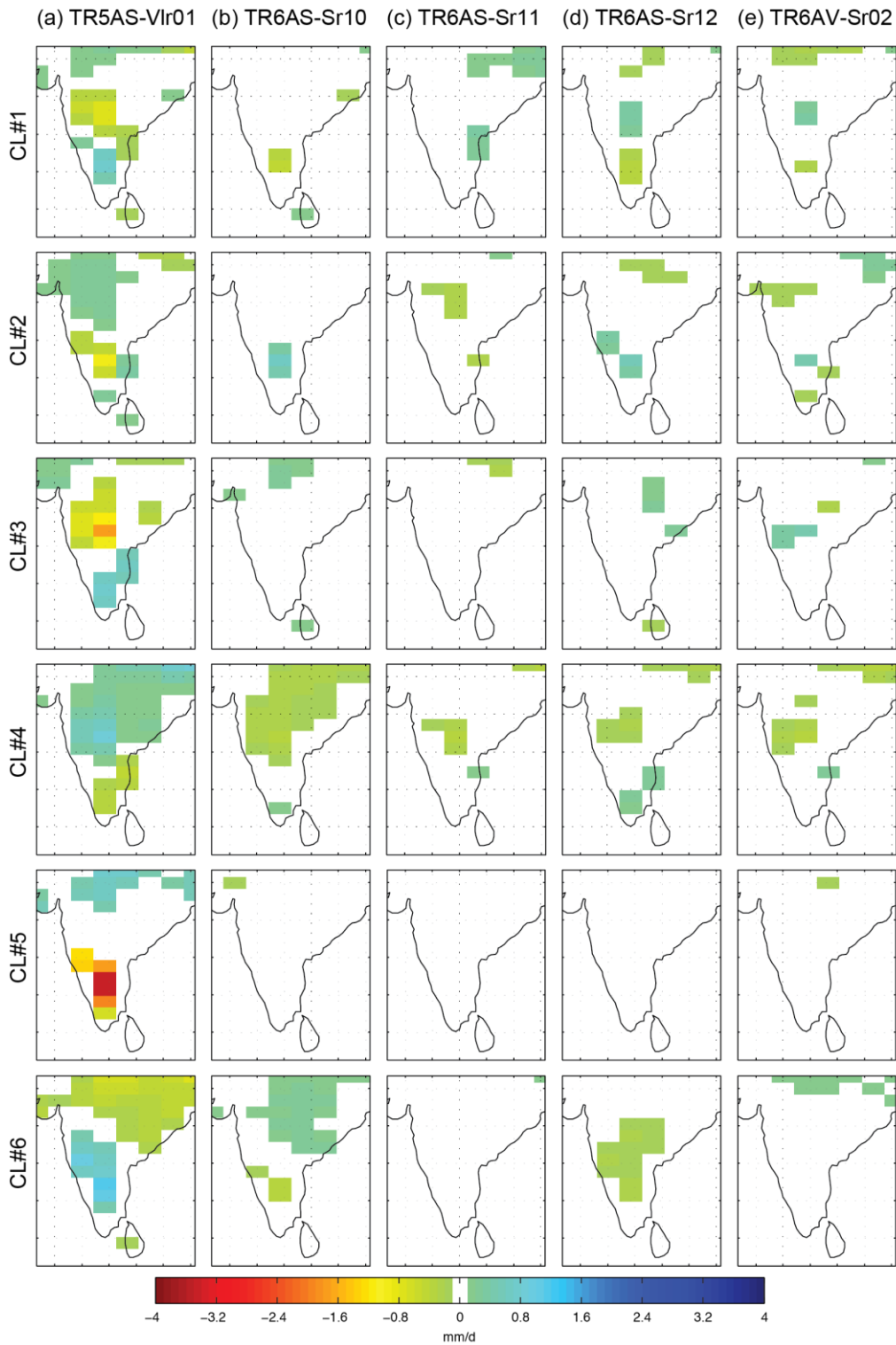
1120  
 1121  
 1122  
 1123  
 1124  
 1125  
 1126

**Figure 9:** Same as Fig. 7 but for 850-hPa wind anomalies (vectors; m/s) and associated divergence (shadings; m/s; blue = anomalous convergence; red = anomalous divergence). Wind anomalies are shown in black when at least one component (i.e., zonal or meridional) depict significant changes tested as in Fig. 7.



1127  
 1128  
 1129  
 1130  
 1131  
 1132  
 1133

**Figure 10:** (a) Ensemble mean rainfall and SST anomalies associated with the six ISMR regimes identified by applying the AHC clustering to the last 100 years (i.e., 1851-1950) of the TR5AS-Vlr01 and TR6AV-Sr02 ensemble. Significant anomalies at the 95% confidence level according to a Student t test are contoured in black. (b) Same as (a) but for the CRU-HadISST data for the 1901-2016 period.



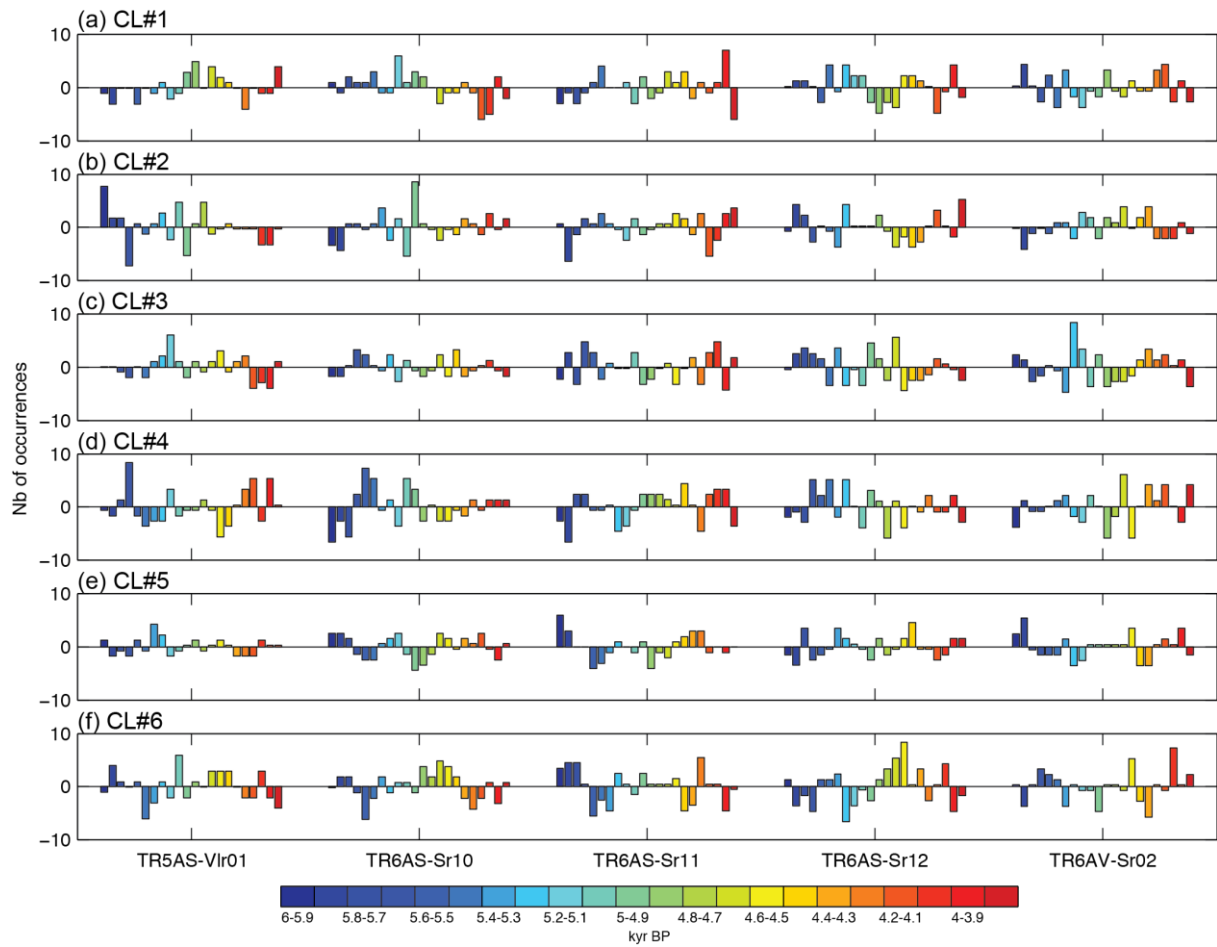
1134

1135

1136 **Figure 11:** Model dependency in the mean anomalous rainfall pattern associated to the six  
 1137 ISMR regimes for (a-e) the five simulations. For each ISMR regime, model dependency is  
 1138 defined as the departure of the mean anomalous rainfall pattern of each simulation from the  
 1139 ensemble mean anomalous rainfall pattern shown in Fig. 7. Only departure significant at the  
 1140 95% confidence level according to a Student t test is shown.

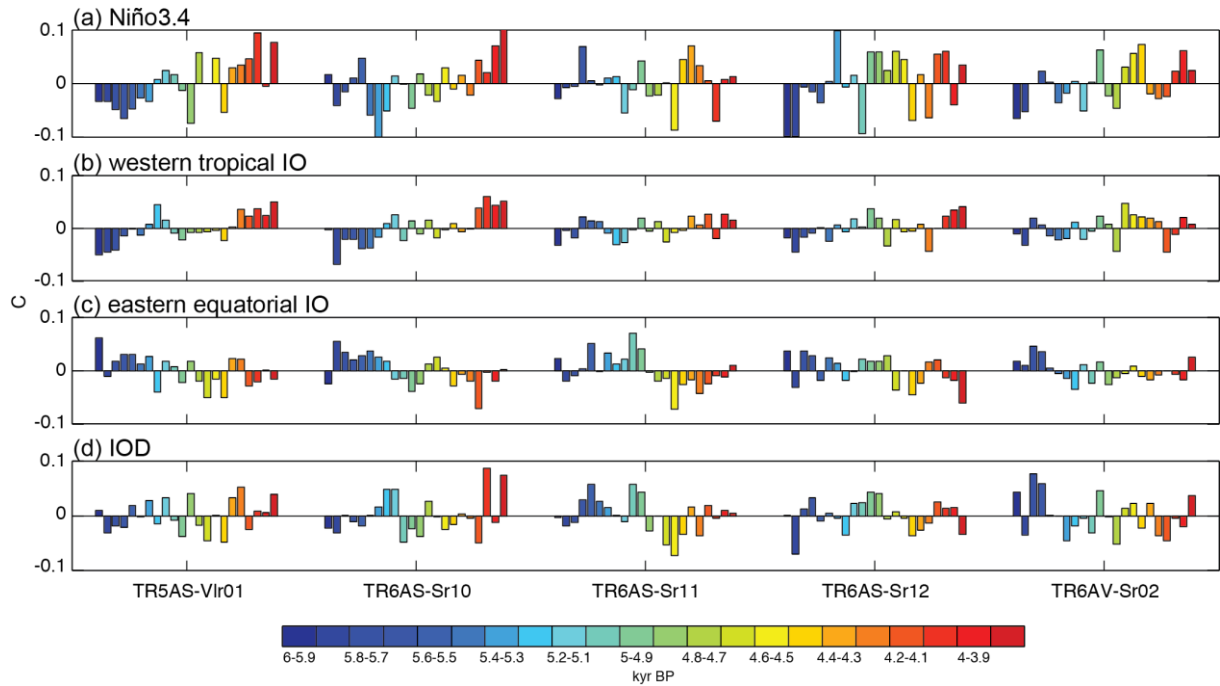
1141





1142  
 1143  
 1144  
 1145  
 1146  
 1147

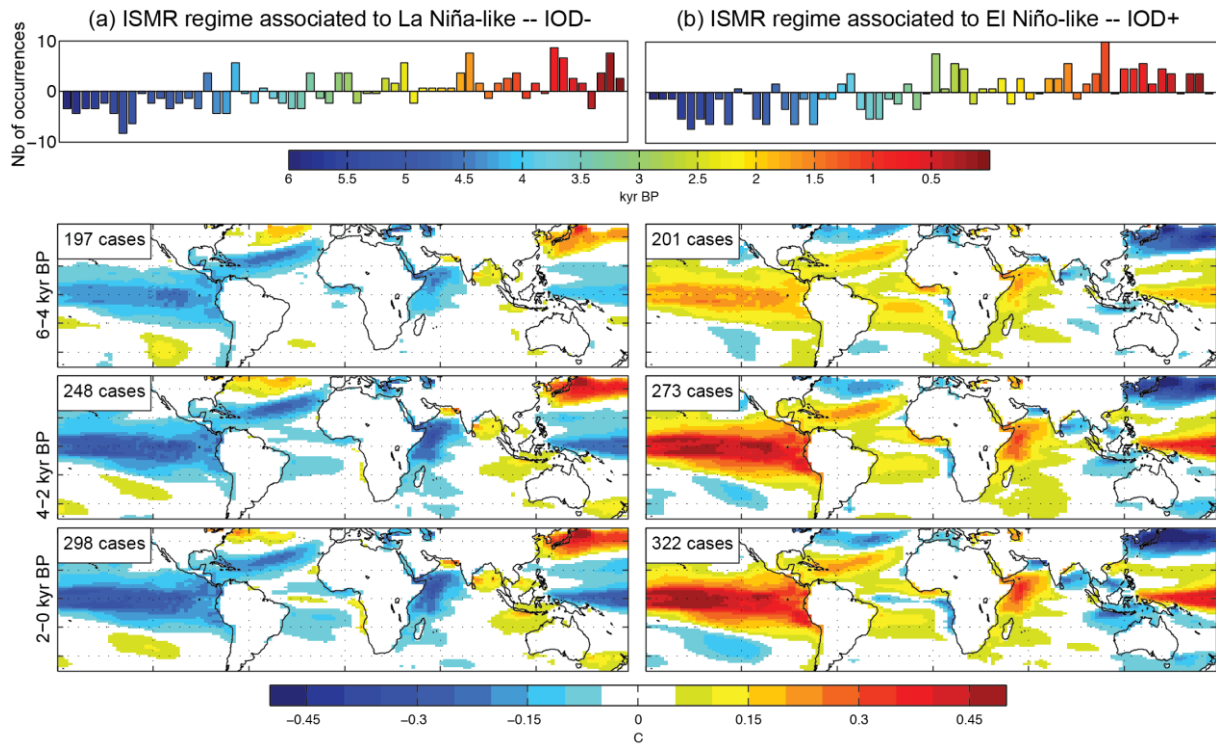
**Figure 12:** (a-f) Century-to-century evolution in the frequency of occurrence of the six ISMR regimes from 6 to 3.8 kyr BP for the five simulations. The frequency of occurrence is expressed as the departure from its mean value.



1148

1149

1150 **Figure 13:** Century-to-century evolution in boreal summer (JJAS) SST variability of the (a)  
 1151 Niño3.4, (b) western tropical IO (10°S-10°N; 50°-70°E), (c) eastern equatorial IO (10°S-Eq;  
 1152 90°-110°E) and (d) IOD indices from 6 to 3.8 kyr BP for the five simulations. Variability is  
 1153 defined as standard-deviation of SST anomalies for each 100-yr adjacent window. The  
 1154 variability is displayed as the departure from the mean value of the standard-deviations  
 1155 computed for each 100-yr adjacent window.



1156

1157

1158

1159

1160

1161

1162

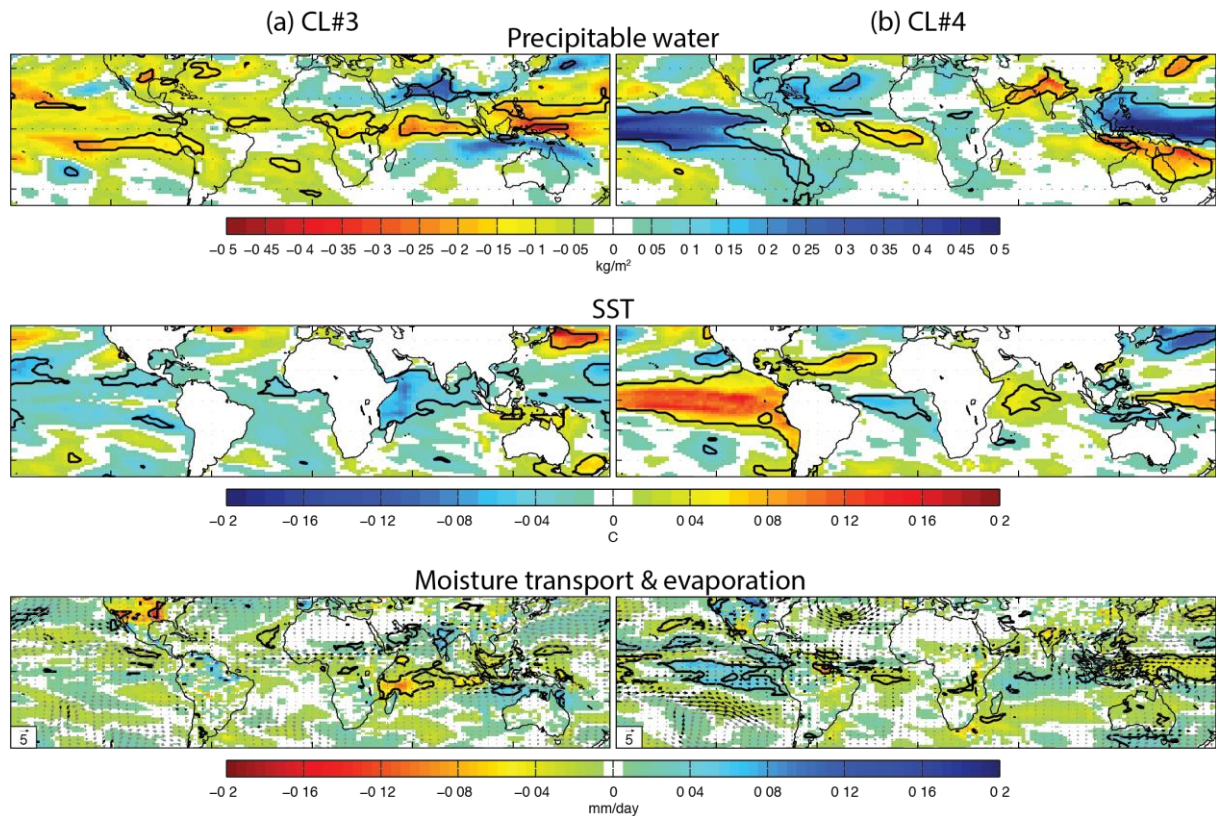
1163

1164

1165

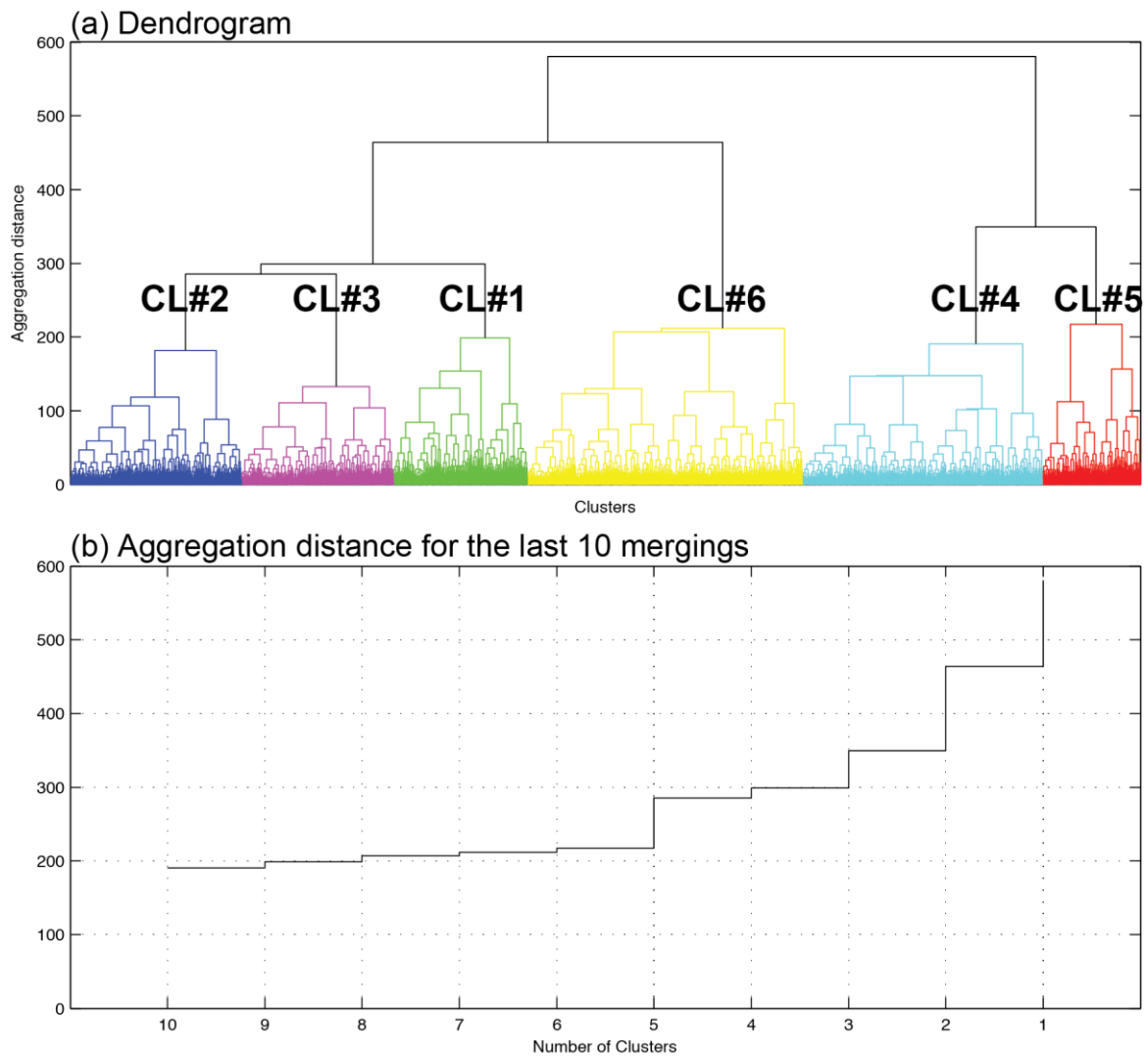
1166

**Figure 14:** (a; upper panel) Century-to-century evolution in the frequency of occurrence of the ISMR regime associated to La Niña-like – IOD- collocation from 6 to 0 kyr BP for the TR6AV-Sr02 simulation. This ISMR regime is extracted by applying the AHC clustering to anomalous Indian rainfall patterns from 6 to 0 kyr BP in the two 6000-yr simulation ensemble (TR5AS-Vlr01 and TR6AV-Sr02) with a 6-regime cutoff. The frequency of occurrence is expressed as the departure from its mean value. (a; bottom panels) Number of occurrences of this ISMR regime along each 2000-yr adjacent window and associated mean anomalous SST patterns. Only SST anomalies significant at the 95% confidence level according to a Student t test are shown. (b) Same as (a) but for the ISMR regime associated to El Niño-like – IOD+ collocation.



1167  
 1168  
 1169  
 1170  
 1171  
 1172  
 1173  
 1174

**Figure 15:** (a) 4.9-3.8 minus 6-4.9 kyr BP differences in precipitable water, SST, moisture transport and evaporation ensemble mean anomalies associated to regime #3. Significant anomalies at the 95% confidence level according to a Student two-tailed t test are contoured in black for precipitable water, SST and evaporation and shown with black vectors for moisture transport. (b) Same as (a) but for regime #4.



1175  
 1176  
 1177  
 1178  
 1179  
 1180

**Figure A1:** (a) Dendrogram tree obtained at the end of the AHC procedure applied to JJAS rainfall anomalies simulated over India by the 5-simulation ensemble from 6 to 3.8 kyr BP. (b) Evolution of the similarity metric for the 10 last mergings. See Appendix A for details.